AN INVESTIGATION ON PREDICTION OF STRETCH EDGE CRACKING IN ADVANCED HIGH STRENGTH STEELS

A Thesis

by

DIVYA MENGJI

Submitted to the Graduate and Professional School of
Texas A&M University
in partial fulfillment of the requirements for the degree of

MASTER OF SCIENCE

Chair of Committee,	Jyhwen Wang
Committee Members,	Amine Benzerga
	Bruce Tai
Head of Department,	Bryan Rasmussen

May 2022

Major Subject: Mechanical Engineering

ABSTRACT

Advanced High Strength Steels (AHSS) are increasingly being used in the automotive industry for vehicle body manufacturing to reduce overall weight and increase fuel efficiency. Major challenges associated with forming AHSS sheets arise due to edge cracking of blanked/trimmed edges that occurs at much lower strains than those predicted by traditional Forming Limit Diagrams (FLDs). In this work a comprehensive experimental and numerical investigation was executed to understand the fracture behavior of AHSS and establish Finite Element Analysis (FEA) model to predict limiting strains. Experimentation involved observation of the effects of sample parameters of single notched samples such as notch radius, material orientation and edge quality, on fracture strains of various AHSS grades. Execution of a general numerical modeling study helped validate and establish anisotropic material modelling technique in ABAQUS code for DP 980 BARE and CR 780 grades. Limiting strains were numerically identified using second time derivative of thickness strain method and compared to experimental results obtained using Digital Image Correlation (DIC) strain analysis.

Edge quality played a critical role in determining formability property of samples while considering various notch radii. The smooth-edge samples showed greater formability with smaller notch radius (higher strain gradient) which contrasted with sheared-edge samples that displayed lower formability for smaller notch radius. Additionally, FEA predicted limiting strains were lower than actual fracture strains for smooth-edge while they were slightly higher for sheared-edge samples. A new Failure Strain Factor was introduced as empirical relation between FEA predicted limiting strains and DIC fracture strains for sheared-edge samples. This testing and FEA prediction method provided conservative results for smooth-edge and favorable results for sheared-edge samples with the use of Failure Strain Factor. Consequently, it was concluded that this method could be useful in metal forming industry for predicting limiting strains for AHSS.

ACKNOWLEDGMENTS

This work was supported by the thesis committee chair Dr Jyhwen Wang, Professor in Manufacturing and Mechanical Engineering Technology, Department of Engineering Technology and Industrial Distribution, Texas A&M University. It was also supported by the valuable work of Michael Kolodziej, Stephen All and Madhur Wadge, previous students in the program, who performed experimental work and DIC analysis of smooth-edge samples. I also wish to acknowledge and thank committee members Dr Amine Benzerga, Professor, Aerospace Engineering & Material Science Engineering and Dr Bruce Tai, Assistant Professor, Mechanical Engineering, Texas A&M University for their support throughout the review process.

The experiments of the sheared-edge samples were conducted with the help of Dr Dinakar Sagapuram and Harshit Chawla utilizing equipment from Department of Industrial and Systems Engineering, Texas A&M University. EDM cutting was performed at Department of Material Science and Engineering and Department of Engineering Technology and Industrial Distribution, Texas A&M University, for smooth-edge and sheared-edge samples, respectively. DIC technology and tensile testing equipment from Department of Aerospace Engineering, Texas A&M University, were also used for training and testing purposes. Furthermore, I would like to thank the Department of Engineering Technology and Industrial Distribution and J Mike Walker 66' Department of Mechanical Engineering at Texas A&M University for providing the opportunity to perform and finish this research work and thesis.

CONTRIBUTORS AND FUNDING SOURCES

Contributors

The EDM cutting, experimental testing of samples and 2D DIC strain analysis of smooth-edged tensile and notched specimens was executed by Michael Kolodziej, Stephen All (undergraduate students) and Madhur Wadge (graduate student).

Funding Sources

This research was partially supported by the National Science Foundation under Grant No. EEC-1659856.

REU Site: Interdisciplinary Research Experiences in Metrology & Non-Destructive Inspection.

Any opinions, findings, and conclusions or recommendations expressed in this material are those of the author(s) and do not necessarily reflect the views of the National Science Foundation.

NOMENCLATURE

AHSS	Advanced High Strength Steels
CP	Complex Phase
CR	Cold Rolled
DIC	Digital Image Correlation
DP	Dual Phase
EDM	Electrical Discharge Machining
EG	Electro-Galvanized
EWF	Essential Work of Fracture
FE	Finite Element
FEA	Finite Element Analysis
FLC	Forming Limit Curve
FLD	Forming Limit Diagram
FLSD	Forming Limit Stress Diagram
HER	Hole Expansion Ratio
HET	Hole Expansion Test
HF	Hot Formed
HSS	High Strength Steels
M-C	Mohr-Coulomb
M-K	Marciniak-Kuczynski
MMC	Modified Mohr-Coulomb
TRIP	Transformation Induced Plasticity

TABLE OF CONTENTS

Page

LIST OF FIGURES

FIGURE Page

LIST OF TABLES

TABLE Page

1. INTRODUCTION

Advanced High Strength Steels abbreviated as "AHSS" are classified as steel grades that possess immensely high yield and tensile strengths compared to conventional steel grades. Their unique micro-structure allows these steels to possess yield strengths going past 300 MPa, and tensile strengths going beyond 500 MPa [1]. They hold multi-phased micro-structure as compared to conventional High Strength Steels (HSS), which are single-phased, and contain retained austenite, martensite and bainite [1]. Due to their light weight and high strengths, these steel sheets are distinctly preferred by the automotive industry for vehicle body manufacturing to reduce body weight and enhance crashworthiness [3].

Although AHSS hold high strengths, they are much less formable than conventional steels. Figure 1.1 (reprinted from [1]), which is also referred to as "Banana Curve" of automotive steels, depicts the decrease in total elongation with increasing strength.

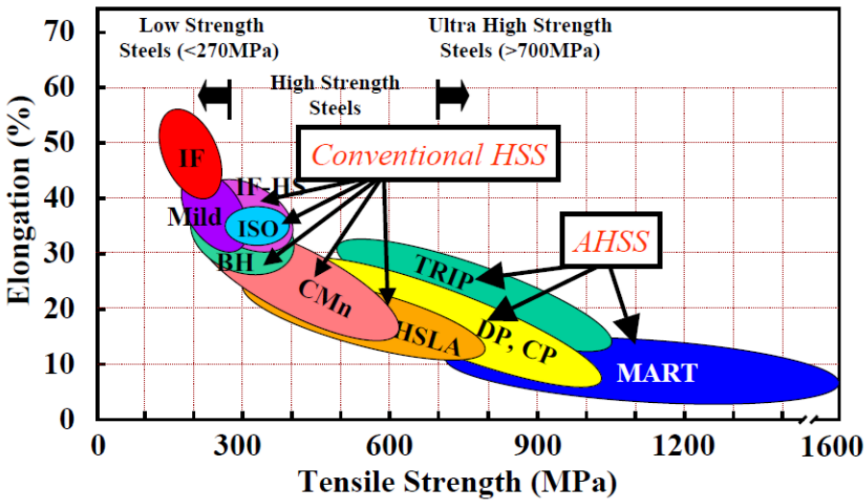

Figure 1.1: % Elongation vs Tensile Strength curve (Reprinted from [1]).

1.1 Challenges in Forming AHSS

The use of higher strength steels in automotive industry has been expanding in consideration of environmental problems to reduce body weight and improve crashworthiness. However, there are several technical issues associated with the use of steel sheets that have poor ductility consequent to higher strength, represented by the steels on the right hand side of the Banana Curve in Figure 1.1. They pose an increased risk of sheet breakage during press forming, which might lead to repeated adjustment of dies and increase the die manufacturing costs [3].

These type of steels are more prone to cracking, than conventional high strength steels, from the portions on edges where stretch flanging or stretch bending work might be applied, hence special care is taken during press forming of AHSS. There have been several studies to perceive the reason for formation of edge cracks which also look into the parameters and material properties that play a critical role in such failure.

Major difficulties in forming AHSS arise due to edge cracking of blanked/trimmed edges that occurs at much lower strains than those predicted by traditional Forming Limit Diagrams (FLDs). The irregularities and impurities in the material also have an effect on necking failure of AHSS which further render the FLDs unavailing. The multi-phased structure and complex manufacturing processes used to create AHSS also make it challenging to determine material properties accurately and they often require new testing methods [1, 3].

Other challenges include tool wear due to large press capacities required for forming and blanking operations along with large spring back action which lead to dimensional inaccuracy and need additional development. The lubricants, tool materials and coatings used while forming AHSS also require careful selection [1, 3].

1.2 Research Objective and Approach

Aim of this research work is to investigate the need for a prediction model to determine failure in AHSS. The effect of material properties, anisotropy, strain gradient, edge geometry and edge quality of AHSS on edge cracking type of fracture, using both experimental and numerical

modelling approaches were explored.

Different AHSS material grades of single notched specimens with three material orientation directions, various notch radii, and edge qualities that are both smooth (with no burrs/micro-cracks) and sheared (or blanked), were tested using tensile tests to observe effect of material properties, notch radius, anisotropy and edge quality respectively. Digital Image Correlation (DIC) was used for strain data collection and analysis.

Numerical material modelling in FEA code ABAQUS/Explicit was performed to establish material modelling technique. Optimal element type, mesh type and mesh density were selected based on mesh sensitivity analyses. The tensile test simulations were conducted prior to single notched test simulations and validated with experimental results to corroborate FEA capability. Single notched test specimens of different radii of curvature were simulated to understand the effect of notch radius and strain gradient.

The thesis itself starts with providing a brief background on Advanced High Strength Steels and their significance to the present automotive industry while addressing the challenges faced by stamping industry in forming AHSS. The predominant problem of edge cracking and the need to research consequent effect of material properties, anisotropy, edge quality, and strain gradient, is explicated. In the chapters preceding the above topics, an explanation of the experimental investigation and numerical modelling techniques employed in this work are elaborately described. Finally, the results and conclusions of the work are presented and summarized.

2. LITERATURE REVIEW

To provide a synopsis of provocations the industry is facing, studies explaining properties of Advanced High Strength Steels, the challenges faced in terms of forming AHSS, steel grade selection, practical challenges in manufacturing environment and selection of forming and blanking methods were conducted. They also reflected upon advantages of AHSS in weight reduction and improving safety and crash-worthiness [1, 3].

Early fracture in AHSS was a predominant phenomenon observed by the automotive sheet forming industry. This type of failure was also referred to as shear fracture and was significantly different from necking failure in conventional steels. It was observed that shear fracture is unique to AHSS and occurs without obvious necking or thinning, parallel to and near the die under both stretching and bending states. Traditional Forming Limit Diagrams (FLDs) could not predict the forming limits accurately for AHSS under stretch bending over small radius. Shear fracture occured at strains much smaller than FLD predicted strains where the ultimate strain of the material at fracture did not reach the strain on forming limit curve [4].

To address this problem and observe the fracture phenomena closely, various studies and new types of testing methods were introduced. Experimental procedures like hole expansion tests [5] with a review on shear edge condition [2], modified tensile tests [6], deep drawing & bending tests [4, 7], side bending tests (flanging) [8], notched and central hole tests [9] were conducted to scrutinize the process parameters such as, die clearance angle, cutting angle, cutting edge geometry, width of stamping, shape of die & piercing tools, clearance variation, blank holder force, bending radii, shear edge condition and the material behavior.

For numerical analysis, several simulations studies were performed based on replicating the experiment itself. In one such study, hole expansion test was simulated [5] while deep drawing, trimming and stretch flanging were simulated in sequence in another. The influence of modelling parameters such as mesh size and shape at flange edge, friction coefficient, punch speed in the simulation, mass scaling, strain rate and thickness gradients were investigated, while pointing

out issues with mesh distortion and sizing. Maximum strains at mesh elements directly along the edge were plotted in FLD for analysis [10]. In addition, studies that performed microvoid growth analysis conducted simulations that accounted for Critical Damage Value (CDV) factor [7]. One study performed simulation variable studies to capture effects of various material models, hardening rules and solvers on simulation results [11].

Theoretical analysis on localized necking of anisotropic sheets was conducted where anisotropy and strain gradient effects were evaluated by introducing strain gradient term in the constitutive equation [12]. Another study performed transformation of fracture locus to the space of principal strains to reveal new branches in the FLD which helped explain shear-induced fracture [13].

Some investigations took the fracture mechanics approach to make use of Essential Work of Fracture (EWF) methodology as a parameter. One such study elucidates problems faced by manufacturers in selecting the right grade of AHSS. It suggests that fracture toughness determined by EWF method is useful in case of stretch flange-ability where EWF is proposed to be used as a parameter to select AHSS grades to avoid cracking while cold forming [14]. A different analysis rationalizes the use of EWF method to understand crack propagation phenomena, stretch falnge-ability and edge cracking issues of AHSS [15].

To understand the nucleation mechanisms and void growth, there were examinations on microstructural damage control. One of the studies developed an analytical model for void evolution and coalescence to predict the damage rate in hole expansion tests of DP and CP steel grades [16].

There were also studies on stress based models to predict forming limits in numerical simulations. In one such work, a methodology was developed to predict forming limits in both stress and strain forms using strain gradient theory of plasticity and M-K approach [17]. A different examination explains how stress based models of DP and TRIP steel grades were in best agreement with experimental HET tests than strain based FLDs [18]. Effects of pre-forming of AHSS on edge cracking were investigated by testing pre-formed steel strips. While pre-forming of edge into a wave shape prepared the material for subsequent edge stretch process in conventional steels, it's applicability to AHSS was found to be limited [19].

One study proposed the use of three different numerical necking based criteria in finite element simulations for prediction of forming strain limits. The first numerical criteria was based on analysis of thickness strain evolution in specimen's central part, the second was based on analysis of second time derivative of thickness strain to identify start of necking and the third relied on damage threshold related with occurrence of necking [20] where ABAQUS/ Explicit software was used to simulate simple sheet stretching tests and predicted FLDs were compared with experiments for validation. The second criteria mentioned above was utilized to validate necking based simulation models used in this research.

3. EXPERIMENTAL INVESTIGATION

In this chapter the details concerning the experimental part of the investigation are explicated. The objective of performing experiments was to observe the failure behavior of various specimens and understand effect of different parameters, such as, material grade, anisotropy, notch radius and edge quality. Additionally, data recorded from these experiments was used in numerical modelling as input parameters and for validation.

This chapter starts with explaining the sample preparation procedure followed by material characterization, analysis on failure behavior of both smooth/machined edge and sheared/blanked edge notched specimens and finally describes major comparisons & conclusions made. Some of the experimental work and strain analysis was performed by previous students in the program of study. Their valuable contribution in the execution of EDM cutting, experimental work of testing of samples and use of 2D DIC for strain analysis of smooth-edged specimens is rightly acknowledged.

3.1 Sample Preparation

For the experimental part of this investigation, tensile test specimens, cut as per ASTM standard dimensions, and single notched specimens of varying radii of curvature, were tested for different steel grades. Tensile test was conducted to capture material properties while the corresponding steel grade's single notched specimen was tested to capture fracture strains and study effect of various sample parameters on these strains.

Specimens were cut from cold rolled steel sheets in three different material orientation directions, the rolling direction or longitudinal direction (L, 0 degrees to rolling direction), transverse to rolling direction (T, 90 degree to rolling direction) and diagonal to rolling direction (D, 45 degrees to rolling direction).

Two different notch edge quality types, smooth edge (EDM cut) and sheared edge (blanked), were studied to observe and compare effects of edge quality. The machined/smooth edge condition notched samples were obtained using electrical discharge machining (EDM), with no burrs or

microcracks on the edge, while the sheared edge condition notched samples were obtained by blanking operation used to punch the holes that formed the notches, susceptible to accumulating burrs and microcracks on the edge. Both smooth and sheared edge notched specimens were cut to the required dimensions from the rolled sheets using wire EDM. In case of sheared-edge samples it was ensured that the EDM tool does not disturb the blanked edge of the notch, to retain the edge quality generated from the blanking process.

3.1.1 Electrical Discharge Machining

EDM is a non-conventional process which utilizes non-contact methods for machining electrically conductive materials. The wire and work piece operate as electrodes with opposite charges while a series of controlled sparks are generated between them to erode the material. This setup is submerged under a dielectric liquid to facilitate vaporization and dissolving of microscopic particles of the work piece material [21].

All steel specimens in this study were cut using wire electrical discharge machining. Two major advantages of using EDM were the potential to cut the stock despite hardness and the ability to attain extremely smooth finish. EDM cutting of smooth-edge specimens was performed by previous students in the program. All stock plates were stacked and machined simultaneously to reduce time and cost of cutting. Similarly, the sheared-edge specimens were cut using the AgieCharmilles machine. It made use of a zinc coated brass wire of 0.01 inch diameter. A variable feed rate, with a maximum speed of 5 mm/min and minimum speed of 0.8 mm/min, was used. The machine automatically changed the feed rate as per geometry of required specimen. Dielectric liquid availed was de-ionized water which does not conduct electricity. Time taken to machine a stockpile of six plates was approximately five hours with one rough pass and variable feed rate.

Figure 3.1 shows the AgieCharmilles machine used to machine sheared-edge specimens and Figure 3.2 displays the EDM process in progress. In Figure 3.2 a faint spark can be seen below the spool box that held the zinc coated brass wire while the stockpile of plates with blanked holes submerged in de-ionized water was being cut.

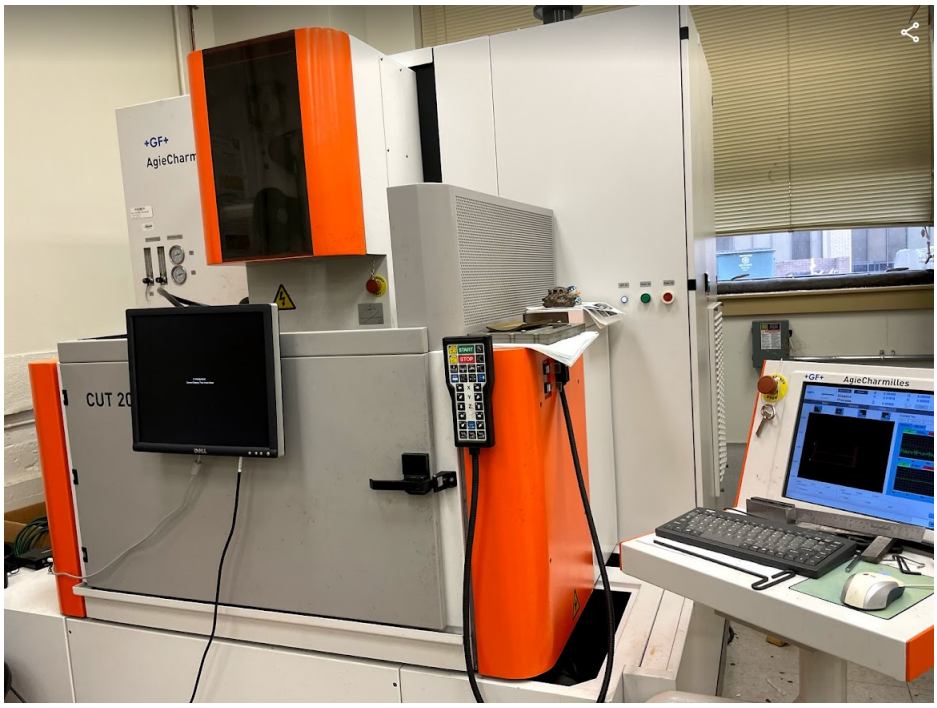

Figure 3.1: Machine used for EDM cutting of sheared-edge specimens.

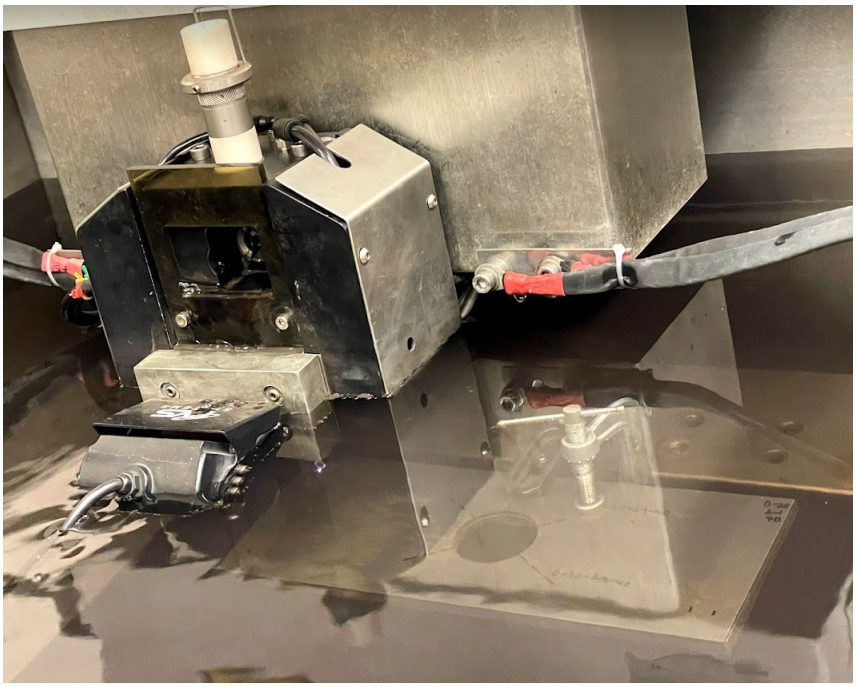

Figure 3.2: EDM cutting in progress for one of the stockpiles of sheared-edge specimens.

3.1.2 Smooth-Edge Condition Specimens

This batch consisted of five steel grades, namely DP 780 BARE, DP 980 BARE, DP 980 EG, 980 HF and 1180 HF. The material, in the form of 30 cm x 30 cm size stock plates of thickness 1.5 mm, were stacked onto each other before they were cut using EDM. Figure 3.3 shows CAD drawing, in SolidWorks software, of the EDM tool path used to cut the required geometry from the square shaped plates. The gauge length of the tensile specimen was 50 mm [22], while three different notch radii of 10 mm, 30 mm, and 50 mm in case of single notched specimens were cut. Figure 3.3 was produced by previous students from the program of study. Figure 3.4 shows the used stock plates after EDM cutting of the smooth-edge samples.

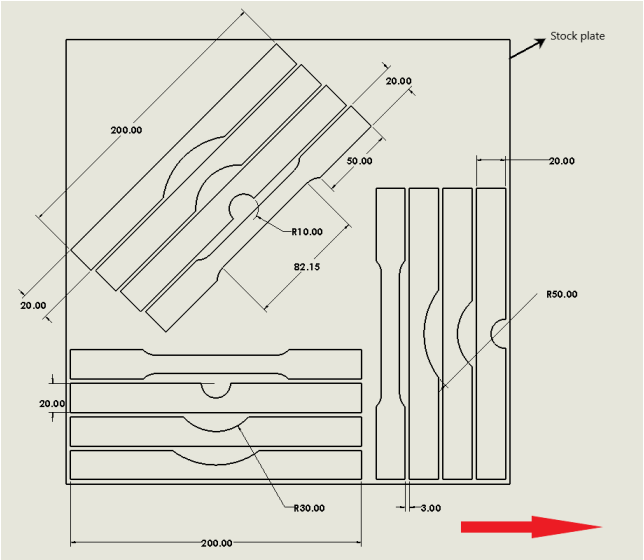

Figure 3.3: SolidWorks drawing of tool path used in wire EDM, rolling direction is represented by the red arrow, tensile and single notched specimens (10mm, 30mm and 50mm radii) were cut in three orientations.

3.1.3 Sheared-Edge Condition Specimens

In case of sheared edge or blanked edge samples, two different steel grades, namely CR 780 and CR 980, with two die clearance values of 20% and 30% of sheet thickness, two notch radii of

5 mm and 20 mm, and three orientations of rolling, transverse and diagonal directions, were cut. Tensile specimens were cut as per ASTM E8/E8M – 16a, Subsize Specimen with a gauge length of 25 mm [22]. Although the notched specimens had sheared notches, the tensile specimens were EDM cut, since these were used to record only material properties.

Figure 3.4: Stock plate for machined edge specimens post EDM cutting.

The stock plates were 25 cm x 10 cm in size and each plate had a blanked hole. The stock plate itself was cut from a large sheet in rolling, transverse, and diagonal directions, hence each plate was used to acquire specimen of specific orientation. Blanking operation with two different die clearance values of 20% and 30% of sheet thickness, were used to make holes of 5 mm and 20 mm radii. Figure 3.5 and Figure 3.6 show sketches, in CAD software SolidWorks, of the stock plate and the EDM tool path (light grey) for sheared-edge samples. The subsize specimens were cut in transverse direction from top and bottom of the plate, while a straight cut along the longitudinal mid-axis was made to generate two single notched specimens and two tensile subsize specimens. Figure 3.7 shows the blanked specimens post EDM cutting process.

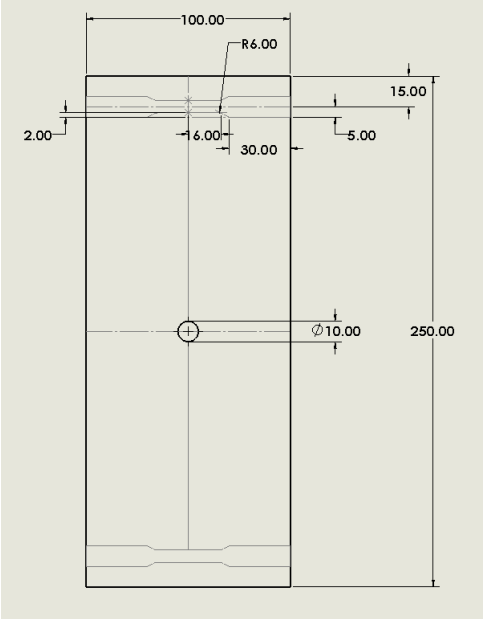

Figure 3.5: SolidWorks drawing of tool path used in wire EDM for 10 mm hole diameter (5 mm notch radius) plate of sheared-edge specimens.

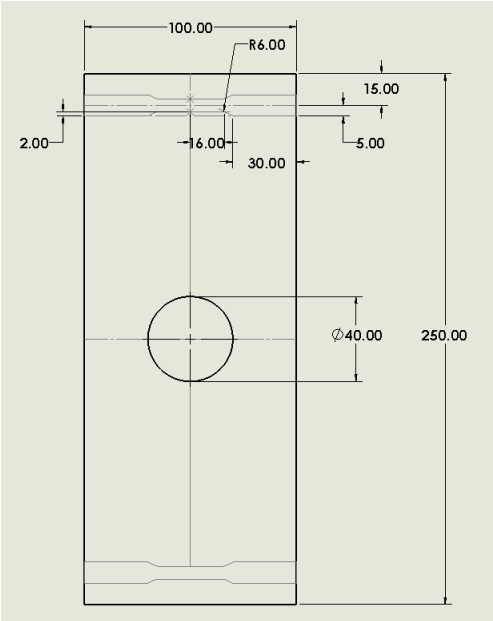

Figure 3.6: SolidWorks drawing of tool path used in wire EDM for 40 mm hole diameter (20 mm notch radius) plate of sheared-edge specimens.

Figure 3.7: Blanked edge specimens post EDM cutting.

3.2 Material Characterization

3.2.1 Digital Image Correlation

Digital Image Correlation (DIC) is a non-contact strain measurement method. The basic principle involves comparison of deformed component image to a reference image, within a field of interest or "Area of Interest". The algorithm for image correlation requires random intensity variations on the surface of interest, hence a speckle pattern is needed on the flat surface which is random enough to show distinguishable patterns at different regions.

In this work, 2D DIC technology was used to measure and capture majorly local strains, along with average strains and displacement data. The software package Correlated Solutions with Vic 2D package was utilized. For sample preparation, a layer of bright (white colored) commercially available spray paint was deposited as background, followed by spraying a layer of dark (black colored) random speckle pattern on the sample. The samples were tested using MTS tensile testing machine. Testing was done when the deposited enamel layers were not entirely dry to prevent peeling of spray paint layers [23]. Similar procedure was followed for single notched specimen

testing.

DIC was chosen as the preferred strain measurement technique over other methods as strains in both horizontal and vertical directions were required. Additionally, local/regional strains were needed to be acquired which was possible only with DIC technology among the available strain measurement methods, such as extensometer, which could only give average strain data in longitudinal direction.

Experiments of smooth-edge and sheared-edge specimens were conducted at different times with separate equipment. The experimental set up for smooth edge specimens consisted of two cameras, one facing the flat surface of prepared samples to be analysed in Vic 2D DIC, while the other placed perpendicular to thickness of specimen to observe necking in thickness direction in both tensile and notched specimens. In case of sheared edge samples, a single camera perpendicular to the flat surface of specimen was installed. The tests were repeated twice to capture pictures in thickness direction during the second repeat, by placing the camera perpendicular to thickness plane.

3.2.2 Tensile Tests

3.2.2.1 Stress vs Strain Behavior of Tensile Specimens (batch consisting of smooth-edged notched specimens)

Material properties were recorded by performing tensile tests of dog-bone specimens cut in three orientations for all five grades of steel. These coupons were cut as per ASTM E8/E8M- 16a standard with gauge length of 50 mm [22]. The true stress vs true strain curves were plotted using strain data analysed with 2D DIC.

The load cell capacity and cross head displacement rate specified in the MTS machine are listed in Table 3.1. Tables 3.2, 3.3 and 3.4 display the values of yield strength, ultimate tensile strength and % elongation that were obtained from the tensile tests for batch consisting of smooth-edge notched specimen steel grades in longitudinal, transverse and diagonal orientations.

Table 3.1: Tensile testing specifications for batch consisting of smooth-edged notched specimens.

Load Cell Capacity	50 KN
Displacement rate for dog-bone specimens	4.929 mm/min
Displacement rate for single notched specimens	4.929 mm/min

Table 3.2: Tensile properties of 0-degree (longitudinal) samples for batch containing smooth-edged notched specimens.

Steel Grade	**Yield Strength(MPa)**	**Ultimate Tensile Strength(MPa)**	**%Elongation**
DP 780 BARE	574.84	890.94	16.89
DP 980 BARE	802.74	1058.16	12.22
DP 980 EG	778.44	1085.89	11.72
980 HF	767.18	1290.42	20.81
1180 HF	1076.90	1405.82	14.18

Table 3.3: Tensile properties of 90-degree (transverse) samples for batch containing smooth-edged notched specimens.

Steel Grade	**Yield Strength(MPa)**	**Ultimate Tensile Strength(MPa)**	**%Elongation**
DP 780 BARE	597.94	899.56	13.84
DP 980 BARE	832.26	1050.91	10.31
980 HF	788.10	1253.30	18.93
1180 HF	1094.84	1413.49	12.65

Table 3.4: Tensile properties of 45-degree (diagonal) samples for batch containing smooth-edged notched specimens.

Steel Grade	**Yield Strength(MPa)**	**Ultimate Tensile Strength(MPa)**	**%Elongation**
DP 780 BARE	595.73	990.80	13.15
DP 980 BARE	815.36	1107.42	13.21
DP 980 EG	755.17	1021.14	9.57
980 HF	775.73	1301.69	20.44
1180 HF	1092.20	1459.62	14.55

Figures 3.8 to 3.12 show the true stress vs true strain plots of the steel grades DP 780 BARE, DP 980 BARE, DP 980 EG, 980 HF and 1180 HF respectively.

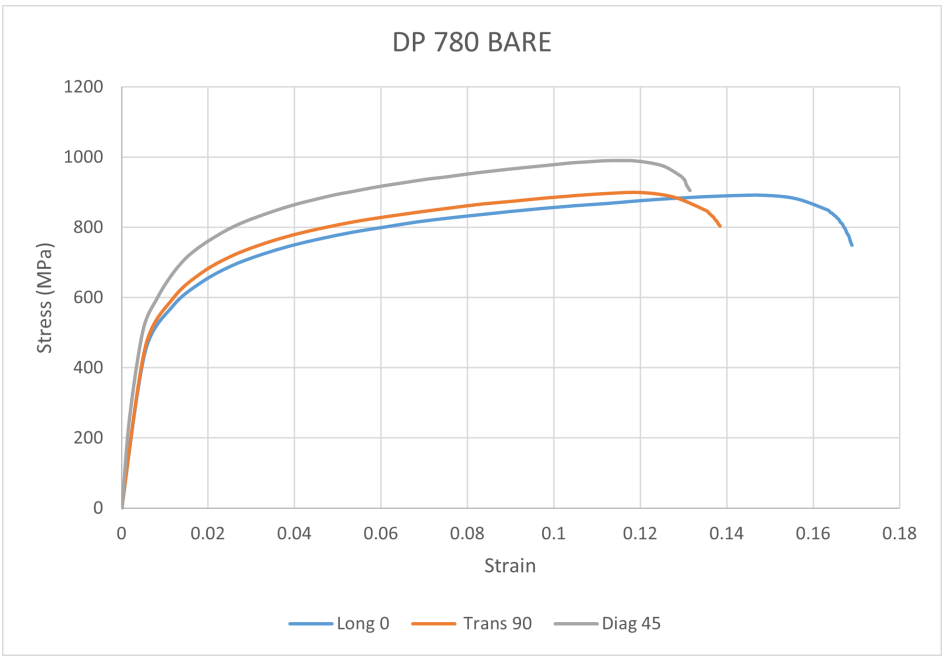

Figure 3.8: True stress-strain plot of DP 780 BARE for three orientations (0,90 and 45 degree).

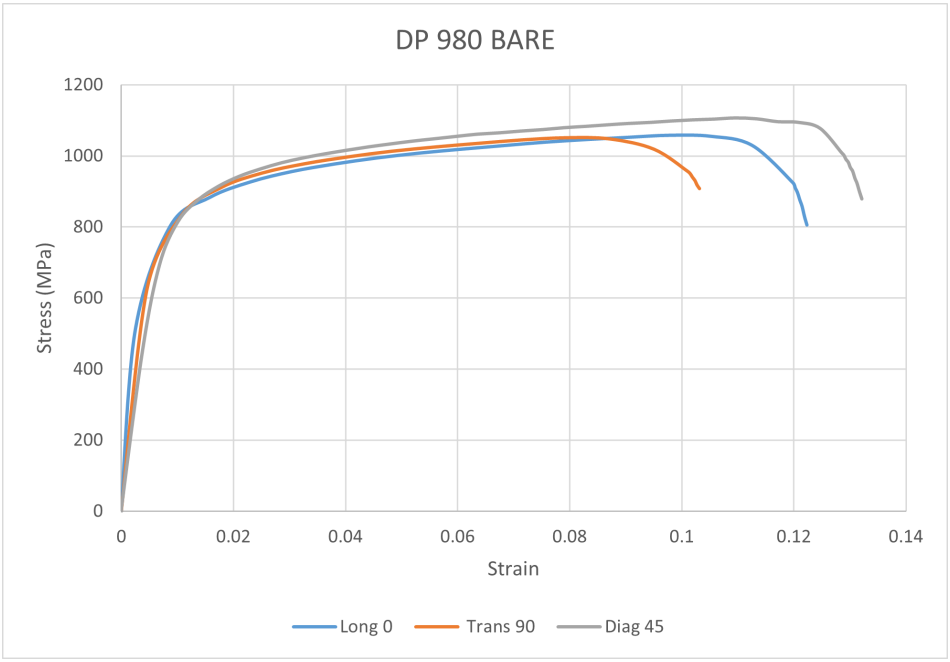

Figure 3.9: True stress-strain plot of 980 HF for three orientations (0,90 and 45 degree).

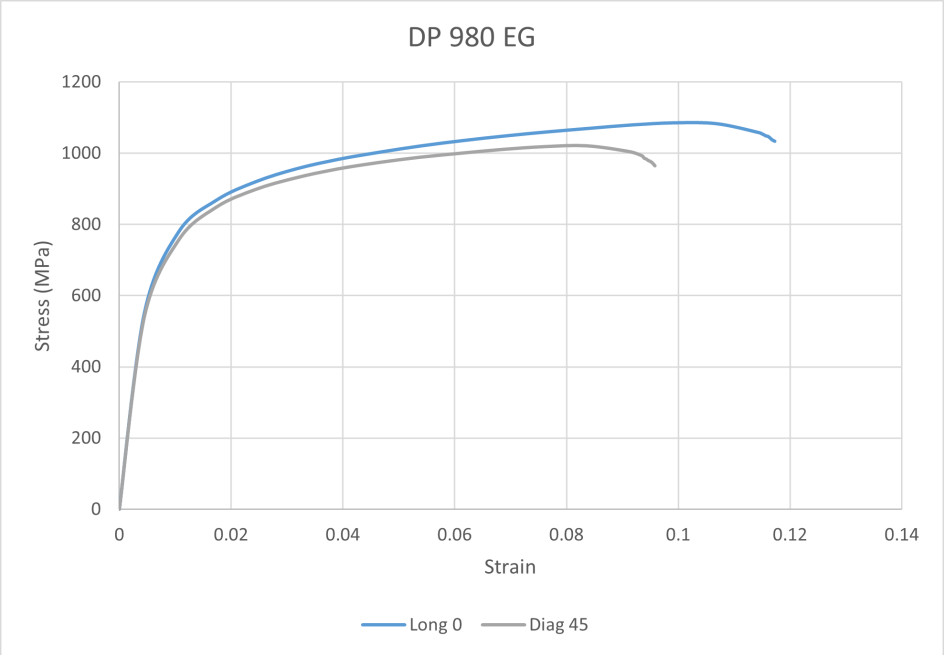

Figure 3.10: True stress-strain plot of DP 980 EG for two orientations (0 and 45 degree).

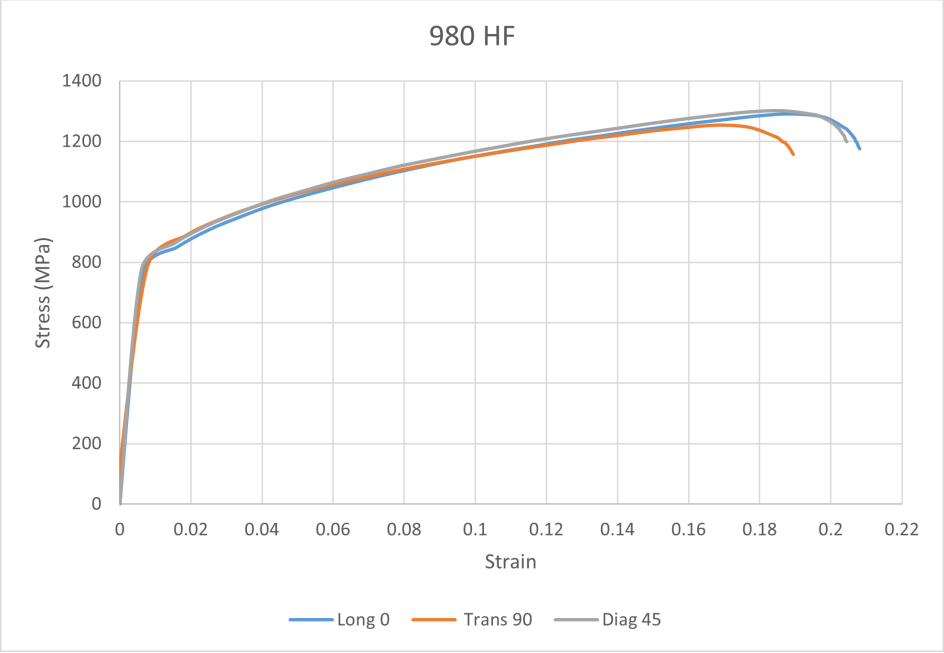

Figure 3.11: True stress-strain plot of DP 980 HF for three orientations (0,90 and 45 degree).

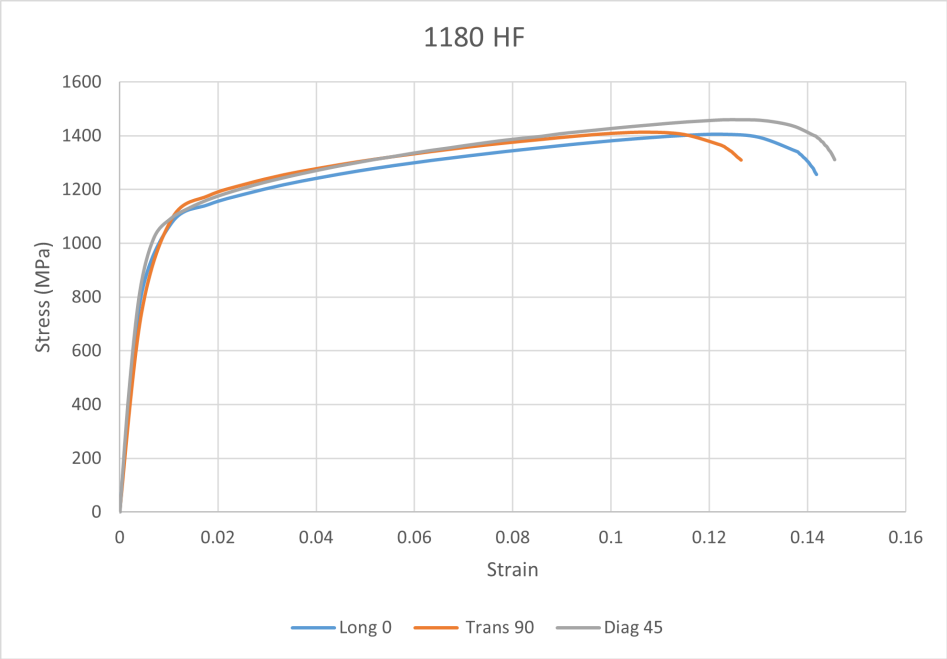

Figure 3.12: True stress-strain plot of 1180 HF for three orientations (0,90 and 45 degree).

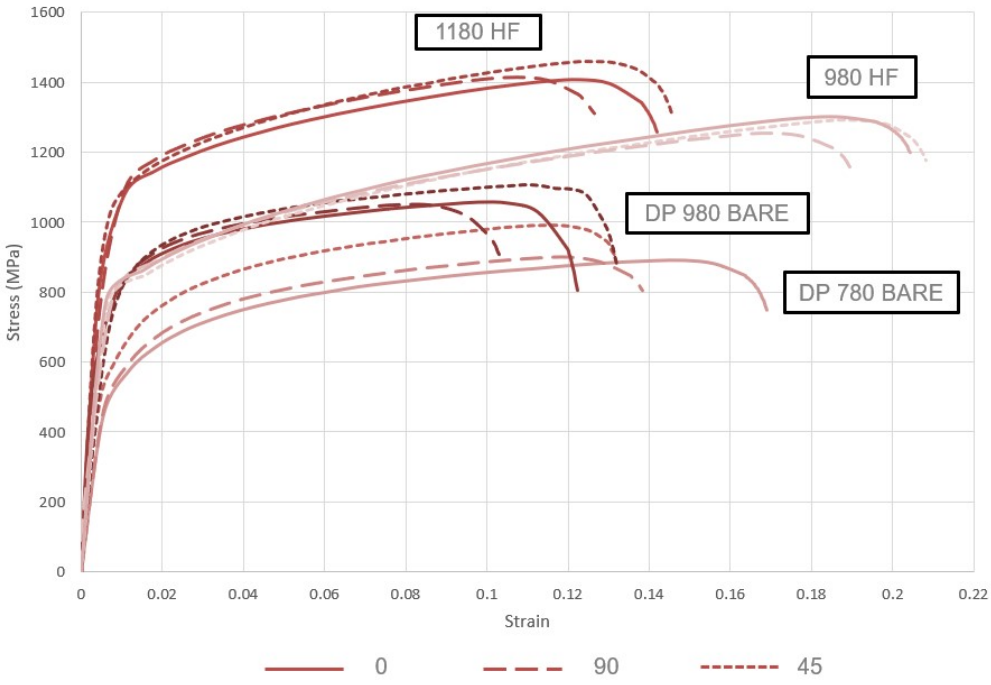

Figure 3.13: True stress-strain plots of smooth-edge specimen steel grades (0,90 and 45 degree).

Figure 3.13 shows all curves in single graph. DP 980 EG was not included in this plot since its properties were close to DP 980 BARE. In case of properties of DP 780 BARE shown in Figure 3.8, it was evidently observed that ultimate tensile strength was lower compared to other steel grades. The 0-degree specimen had highest ductility, whereas 45-degree specimen showed higher toughness property. The 90-degree specimen had lowest ductility and toughness when compared to others. Figure 3.9 shows the curves obtained for DP 980 BARE. It was observed that the 45-degree specimen had highest ductility and toughness property, followed by 0-degree and 90-degree specimens. Additionally, it was noted that the three curves overlap at a point post elastic deformation near yield point. Therefore, the values of yield strength were close for the three orientation types. Figure 3.10 shows properties for 980 EG. It was noted that both 0-degree and 45-degree specimens held very close yield strength while the 0-degree specimen had higher ductility and toughness value. Figure 3.11 displays the stress-strain curve of 980 HF, where the 0-degree and 45-degree specimen curves are extremely close, with almost the same value of failure strain. These also possessed the highest ductility and toughness property, followed by 90-degree specimen. Finally, Figure 3.12 displays properties of 1180 HF. It was observed that the 45-degree specimen has highest ductility property followed by 0-degree and 90-degree ones. It also possessed the highest toughness property followed by the 90-degree and 0-degree specimens.

3.2.2.2 Stress vs Strain Behavior of Tensile Specimens (batch consisting of sheared-edged notched specimens)

In case of sheared/blanked edge, two different steel grades, CR 780 and CR 980 were tested. Tensile tests were conducted on dog-bone specimens which were cut using EDM, as per the sub-size standard for ASTM E8/E8M – 16a with a gauge length of 25 mm [22]. Although this batch contained sheared/blanked notched samples, the tensile test specimens were smooth edged. These tests were conducted to capture materials properties of steel grades used in sheared/blanked notch edge specimens. Table 3.5 lists the specifications of MTS testing machine while tensile testing. The load cell capacity and displacement rate of the cross-head are shown. A lower strain rate was chosen in case of tensile tests to obtain higher number of data points. Tables 3.6, 3.7 and 3.8

display the values of yield strength, ultimate tensile strength and % elongation obtained from the tensile tests of the steel grades used in longitudinal, transverse and diagonal orientations.

Table 3.5: Tensile testing specifications for batch consisting of sheared-edge notched specimens.

Load Cell Capacity	30 KN
Displacement rate for dog-bone specimens	0.48 mm/min
Displacement rate for single notched specimens	6 mm/min

Table 3.6: Tensile properties of 0-degree (longitudinal) samples for batch containing sheared edge notched specimens.

Steel Grade	**Yield Strength(MPa)**	**Ultimate Tensile Strength(MPa)**	**%Elongation**
CR 980	713.07	973.55	11.30

Table 3.7: Tensile properties of 90-degree (transverse) samples for batch containing sheared edge notched specimens.

Steel Grade	**Yield Strength(MPa)**	**Ultimate Tensile Strength(MPa)**	**%Elongation**
CR 780	435.31	886.68	16.26
CR 980	663.62	1008.63	13.74

Table 3.8: Tensile properties of 45-degree (diagonal) samples for batch containing sheared edge notched specimens.

Steel Grade	**Yield Strength(MPa)**	**Ultimate Tensile Strength(MPa)**	**%Elongation**
CR 780	389.53	825.45	15.81
CR 980	669.88	957.91	12.63

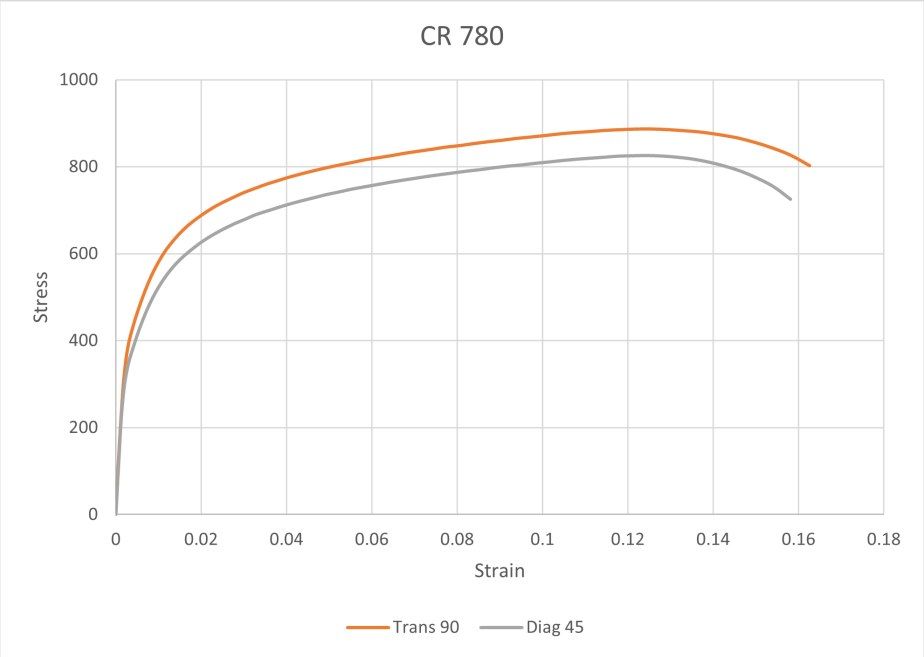

Figure 3.14: True stress-strain plot of CR 780 for two orientations (90 and 45 degree).

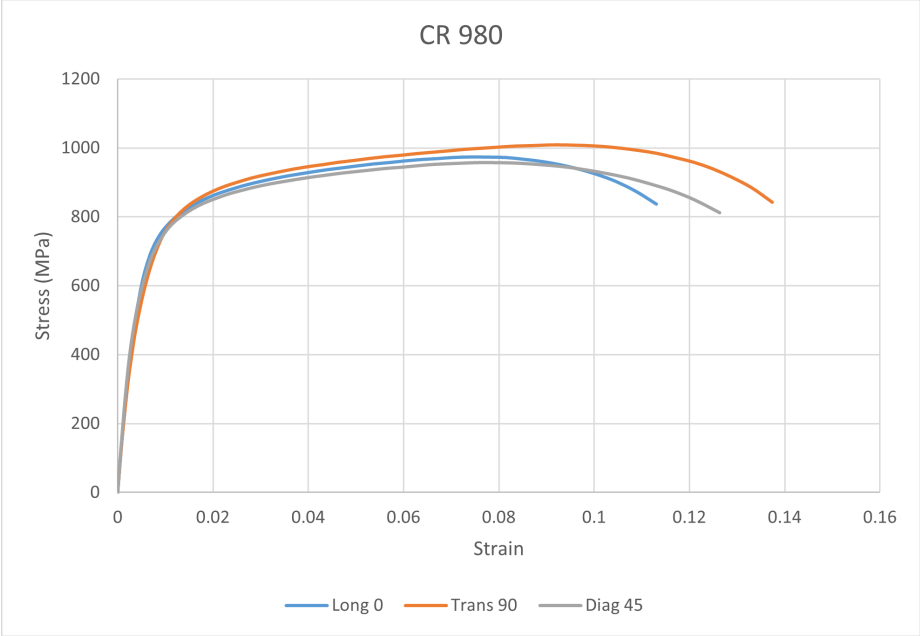

Figure 3.15: True stress-strain plot of CR 980 for all three orientations (0,90 and 45 degree).

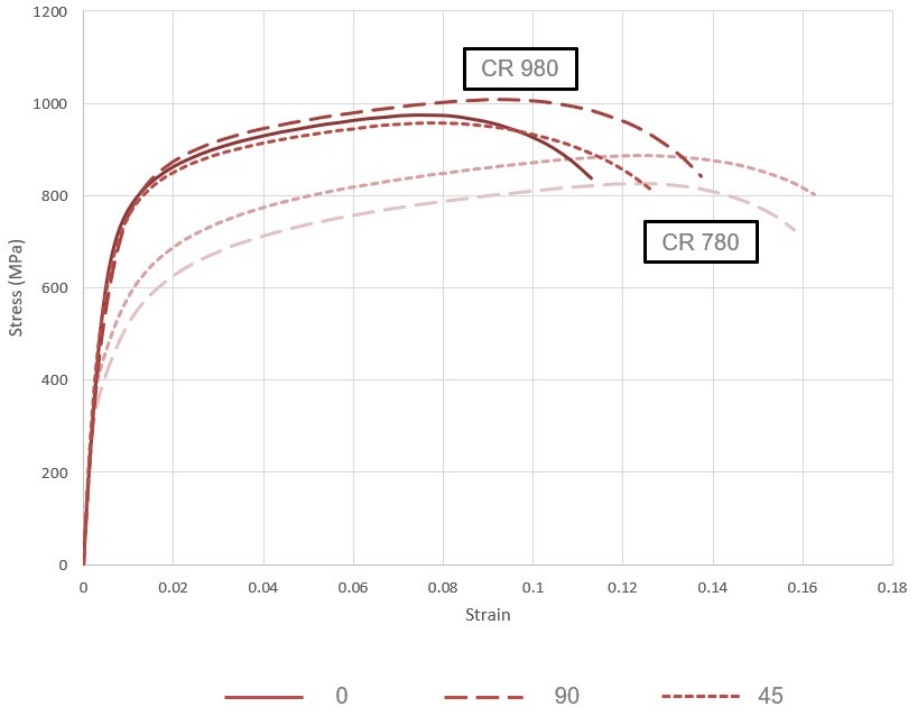

Figure 3.16: True stress-strain plots of sheared edge specimens (0,90 and 45 degree).

Figure 3.14 and Figure 3.15 show the true stress-strain plots obtained from tensile testing, Figure 3.16 shows both plots in a single graph. In case of CR 780, the 90-degree and 45-degree specimens possessed similar ductility property and the 90-degree samples held higher toughness. The curves for CR 980 almost overlap and the 90-degree specimen had highest toughness property followed by 45-degree and 0-degree samples.

3.2.3 Anisotropy

Anisotropy for all steel grades was characterized by calculating the Lankford parameter (*r* value) for specimens cut in three orientations, 0-degree (rolling direction), 90-degree (transverse direction) and 45-degree (diagonal direction) separately, using 2D DIC. Strain in width and length directions were extracted discretely while strain in thickness direction was computed using volume constancy property, as shown in Equation 3.1 and Lankford parameter was computed using Equation 3.2. Here e_{xx}, e_{yy} and e_{zz} represent strains in width, length and thickness directions respectively, of the tensile specimen, in the region where necking had occurred before fracture.

$$e_{xx} + e_{yy} + e_{zz} = 0 \tag{3.1}$$

$$r = \frac{e_{xx}}{e_{zz}} \tag{3.2}$$

Table 3.9 presents individual *r* values for the three orientations of the five steel grades tested using tensile specimens with 50 mm gauge length and Table 3.10 presents same results for the two steel grades tested using tensile specimens with 25 mm gauge length. These were recorded at point of maximum load (at UTS) of the tensile specimens for corresponding material grades. Figure 3.17 shows the method used to compute the strains. A small window was chosen as the area of interest on the picture captured when the specimen was subjected to maximum load. This window was chosen in the region where necking had occurred later in the test.

Table 3.9: Lankford parameter (*r*) values of tensile specimens with 50 mm gauge length at UTS.

Steel Grade	$\mathbf{r_0}$	$\mathbf{r_{90}}$	$\mathbf{r_{45}}$
DP 780 BARE	0.85	0.95	0.69
DP 980 BARE	0.79	0.98	1.03
DP 980 EG	0.83	0.92	0.78
980 HF	0.81	0.91	0.85
1180 HF	0.81	0.93	0.96

Table 3.10: Lankford parameter (*r*) values of tensile specimens with 25 mm gauge length at UTS.

Steel Grade	$\mathbf{r_0}$	$\mathbf{r_{90}}$	$\mathbf{r_{45}}$
CR 780	0.88	0.92	0.75
CR 980	0.73	1.07	1.01

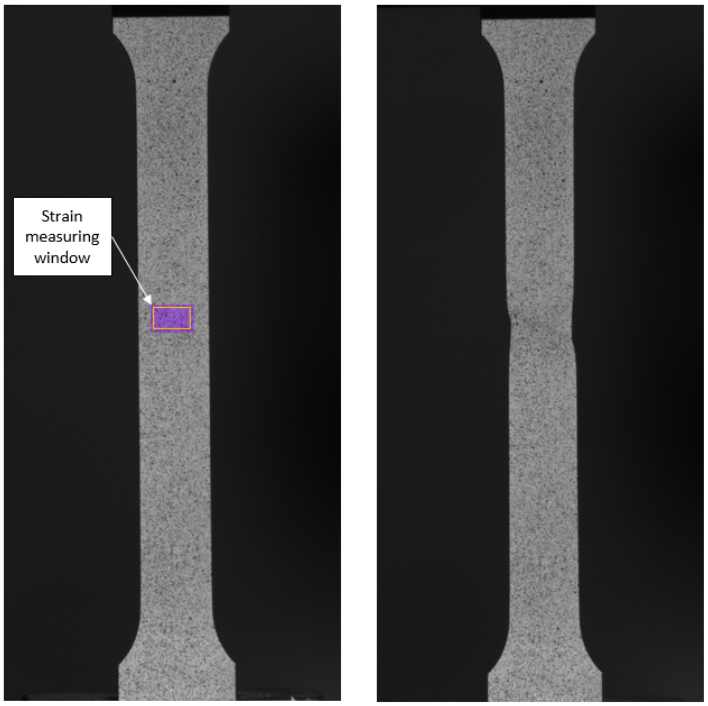

Figure 3.17: Strain measuring method in DIC for computing Lankford parameter, to be provided in ABAQUS as input

3.3 Single Notched Specimen Tests

3.3.1 Smooth-Edge Condition Specimens

Single notched specimens with smooth/machined notched edge were tested for the five material grades. Data was collected from DIC analysis where local strains were captured at the point of fracture and various plots were made for observation and interpretation of fracture behavior. The width of all specimens was consistent at 10 mm, representing the distance from the apex of the notch to the opposite edge. Three parameters identified for observation were notch radius, type of steel grade and material orientation.

Figures 3.18, 3.19 and 3.20 show the variation of major and minor fracture strains, e_{yy} and e_{xx}, as the three parameters, notch radius, steel grade and material orientation vary, respectively.

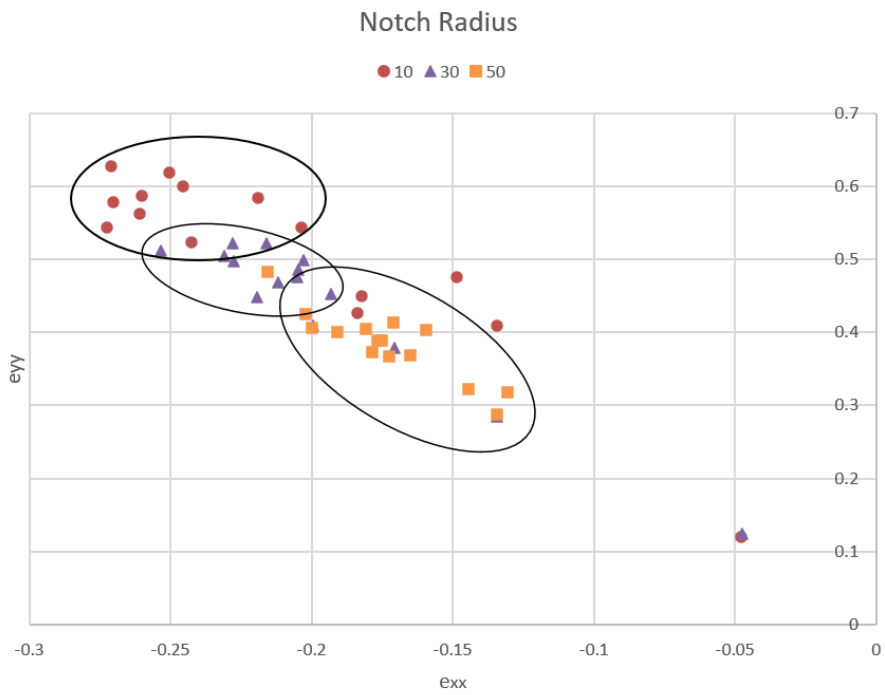

Figure 3.18: Effect of notch radius on smooth edged notched specimens.

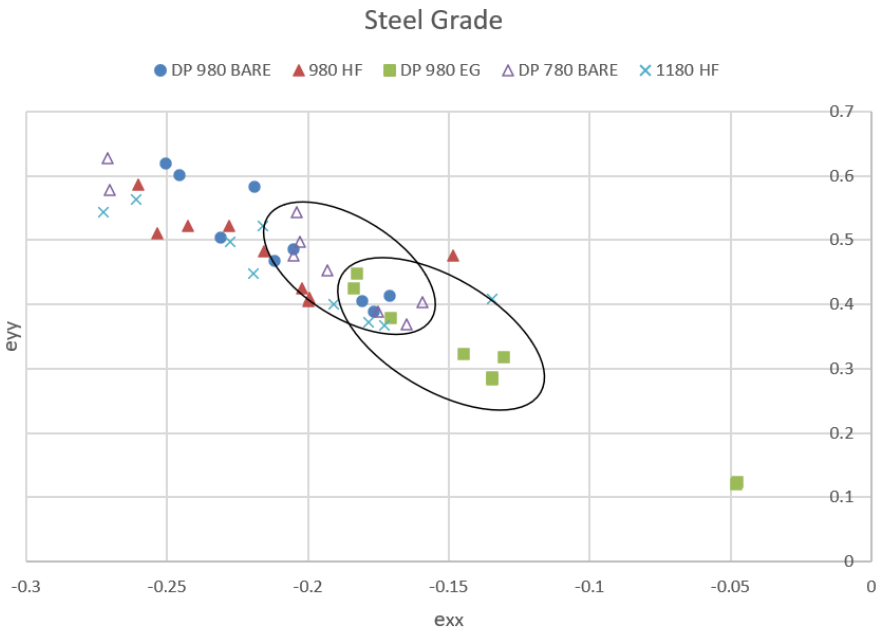

Figure 3.19: Effect of steel grade on smooth edged notched specimens.

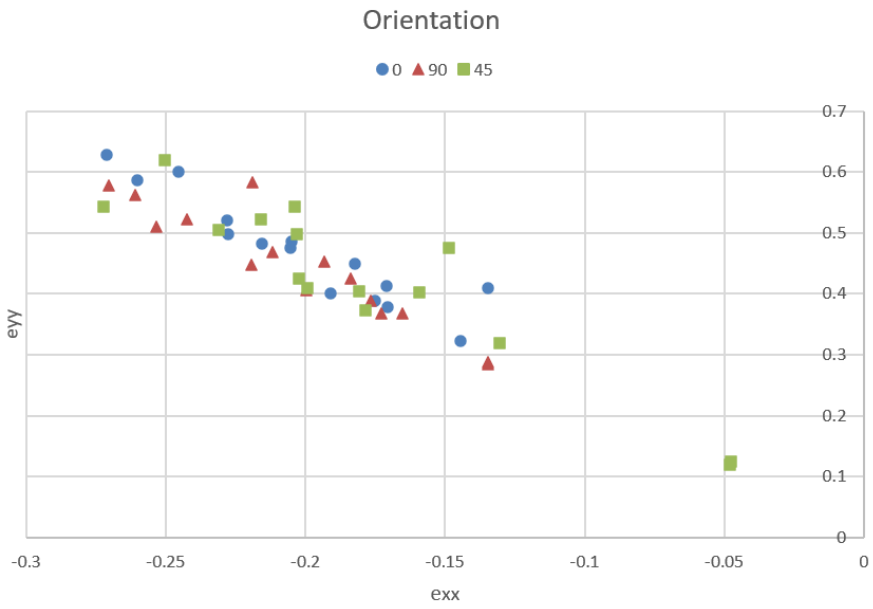

Figure 3.20: Effect of material orientation on smooth edged notched specimens.

A discernible pattern was seen in Figure 3.18 where maximum number of red colored points were situated on the top-left region, the purple triangles lied in between red points and the orange colored squares. Therefore, the sequence of higher fracture strains was 10 mm notch radius > 30 mm notch radius > 50 mm notch radius. To understand the effect of strain gradient and its relation to the notch radius variation, the longitudinal strains, e_{yy} were plotted against the distance from apex along the circumference of the notch, as shown in Figure 3.21. Figure 3.22 shows the strain gradient plot for DP 980 BARE, 0-degree specimen. It was noted that the 10 mm notch radius sample had higher strain gradient than 30 mm samples, followed by the 50 mm notch radius sample. Therefore, a higher strain gradient corresponded to higher fracture strain which in turn corresponded to better formability.

In Figure 3.19, it was observed that maximum number of green colored squares lie at the bottom right side and the hollow purple triangles are clustered at the centre. This signified that DP 980 EG fractured at lower strains compared to other grades, while fracture strains of DP 780 BARE lied at the centre of this plot. To corroborate fracture strains for DP 980 EG, subplots were made for each notch radius and orientation type, while varying the material.

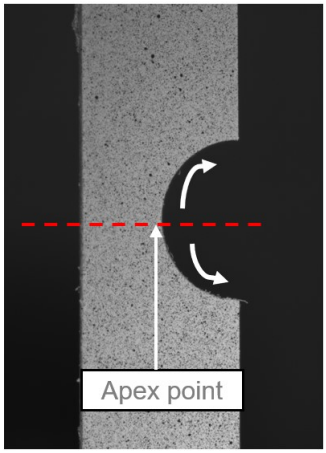

Figure 3.21: Strain gradient measurement from apex along the circumference of the edge.

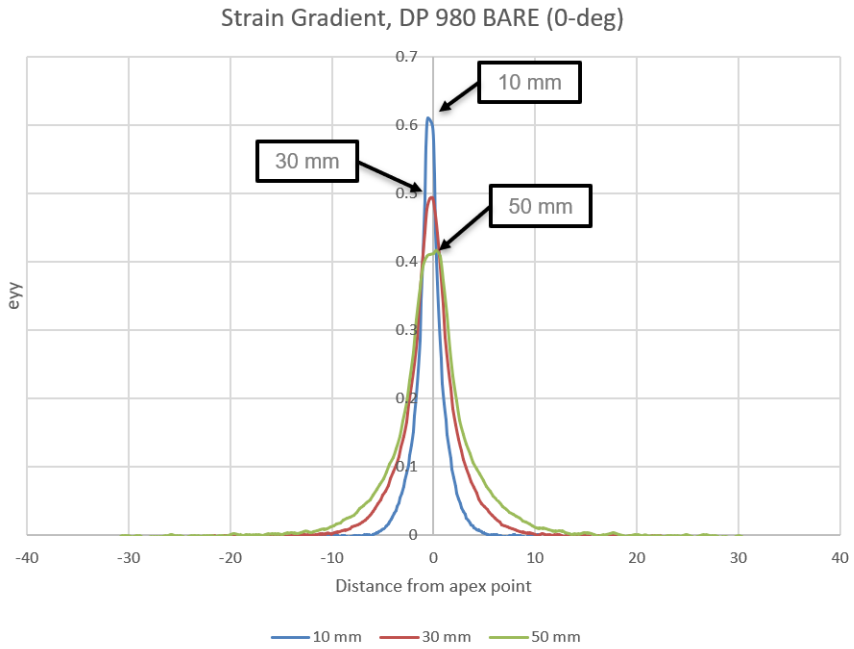

Figure 3.22: Effect of strain gradient for 10 mm, 30 mm and 50 mm notch radius samples.

It was observed that 8 out of 9 subplots showed DP 980 EG fracturing at lowest strains.

From Figure 3.20, no distinct pattern could be remarked, hence sub-plots were made to identify effect of orientation on specific notch radius and material grade. The subplot for DP 980 BARE is shown in Figure 3.23. The graph on the top shows effect of orientation where it was discerned that

the red colored triangles representing 90-degree specimens, fractured at lower strains compared to 0-degree and 45-degree specimens of same notch radius. This observation was corroborated from a study [2] wherein first crack appeared at the edges of the hole, parallel to the material rolling direction in a hole expansion test. The initial crack that appeared parallel to rolling direction corresponded to the 90-degree single notched specimen, as depicted in Figure 3.24 (modified from [2]), fracturing at lower major and minor strains compared to 0-degree and 45-degree samples.

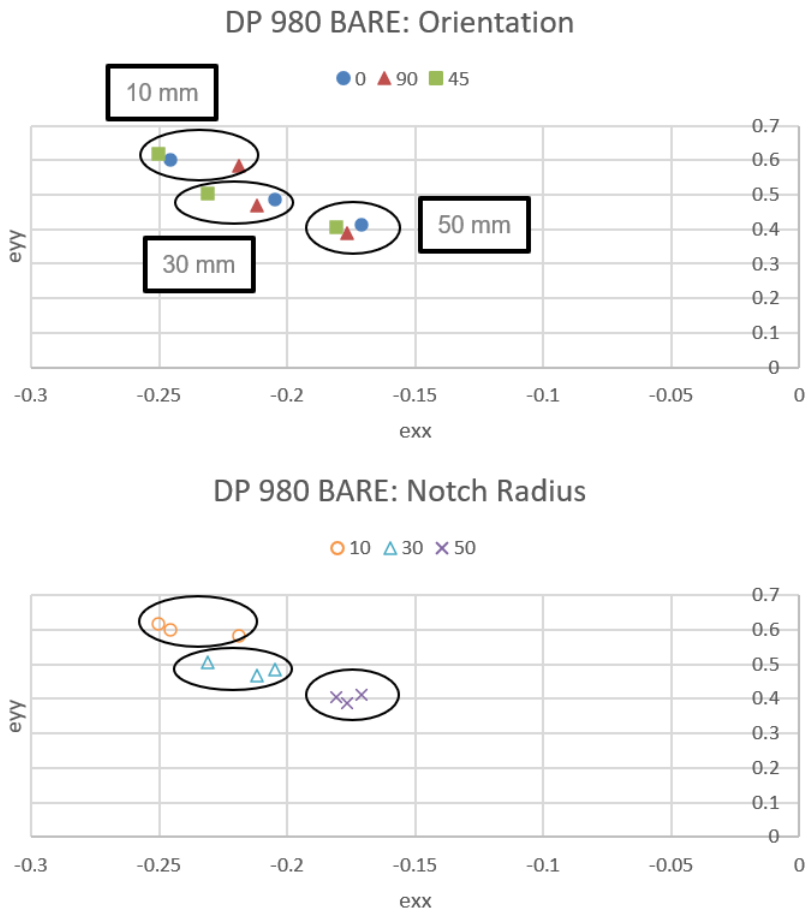

Figure 3.23: Effect of orientation and notch radii in DP 980 BARE.

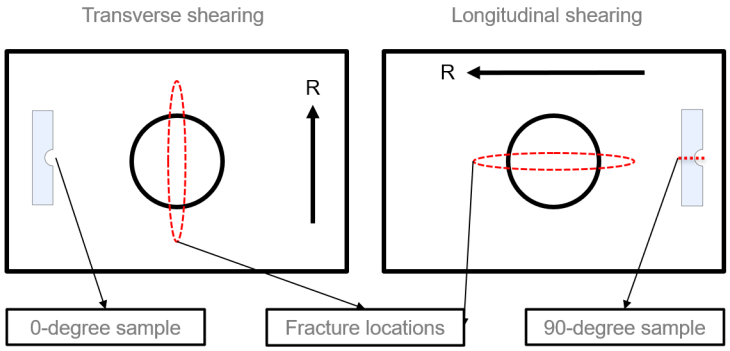

Figure 3.24: 90-degree fractures at lower strain compared to 0-degree specimen corresponding to appearance of initial fracture location in HET (Modified from [2]).

3.3.2 Sheared-Edge Condition Specimens

Single notched specimens with blanked/sheared edge condition were tested for two material grades namely CR 780 and CR 980. Two die clearance values of 20% and 30% sheet thickness and two notch radii of 5 mm and 20 mm, were used. The specimens were pulled using tensile testing equipment while pictures of the width and thickness sections were captured for observation and interpretation of fracture behavior.

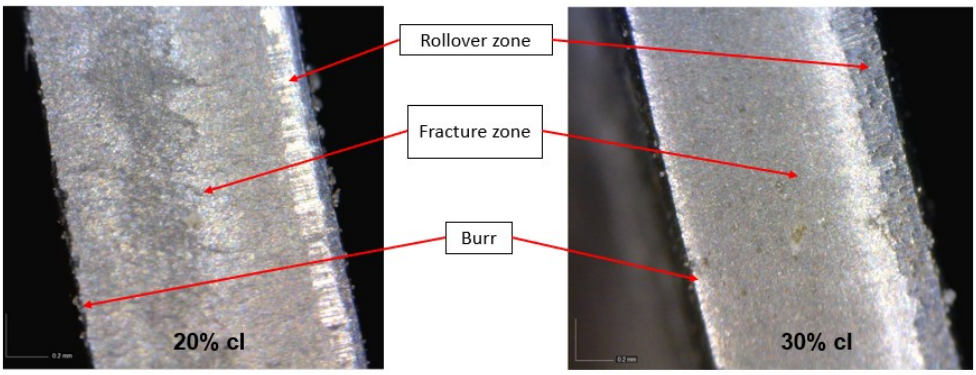

Figure 3.25: Notched edge condition at 20% and 30% of sheet thickness die clearance, 220x magnification.

The width of all specimens was consistent at 15 mm, representing the distance from the apex of

the notch to the opposite edge. Critical parameters identified in case of blanked edge samples were the notch radius, steel grade, material orientation and die clearance values. Figure 3.25 shows the edge condition for 20% and 30% of sheet thickness die clearance values captured under a digital microscope with 220x magnification. The rollover zone, fracture zone and burr are shown.

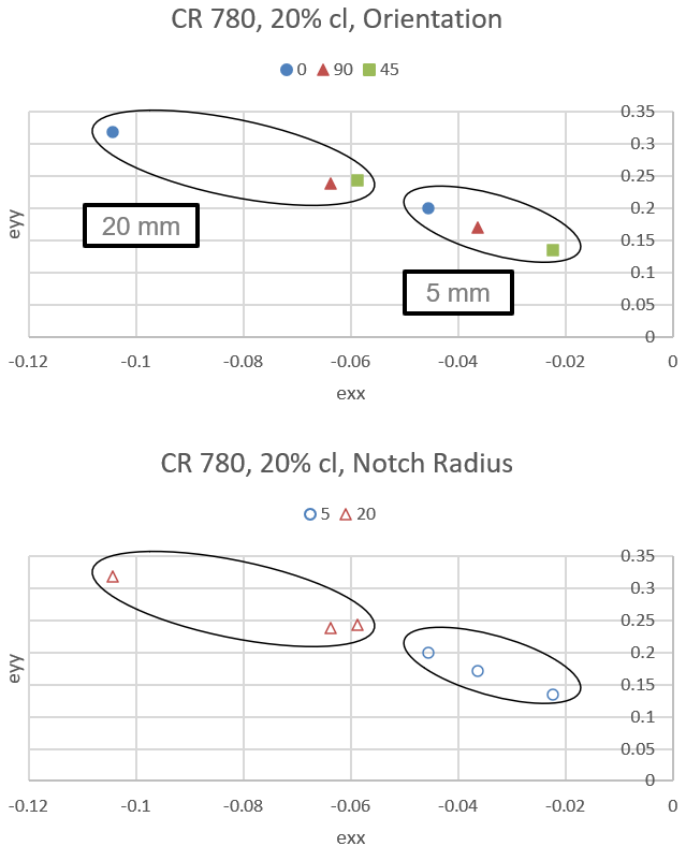

Figure 3.26: Effect of orientation and notch radius in CR 780 (20% of sheet thickness die clearance)

Effect of notch radius and material orientation for CR 780 steel grade with both die clearance values are depicted in Figure 3.26 and Figure 3.27. A critical observation made pertaining to effect of notch radius was that the 20 mm notch radius sample was better than the 5 mm one in terms of formability. The same was true for both 20% and 30% of sheet thickness, die clearance value samples, which contrasts with the trend observed in smooth-edged samples.

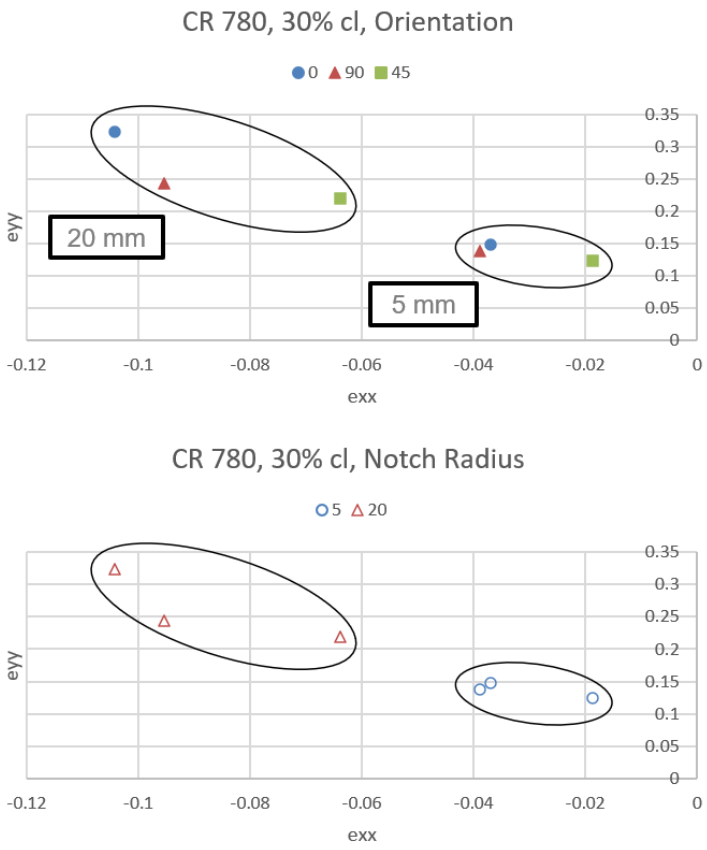

Figure 3.27: Effect of orientation and notch radius in CR 780 (30% of sheet thickness die clearance)

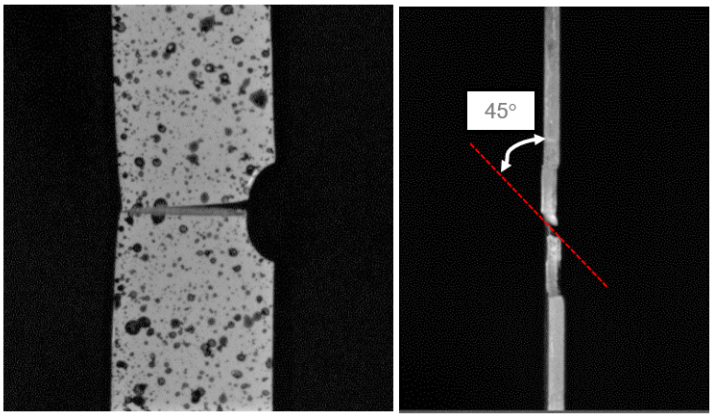

Figure 3.28: 45-degree crack observed in thickness plane (5 mm notch radius).

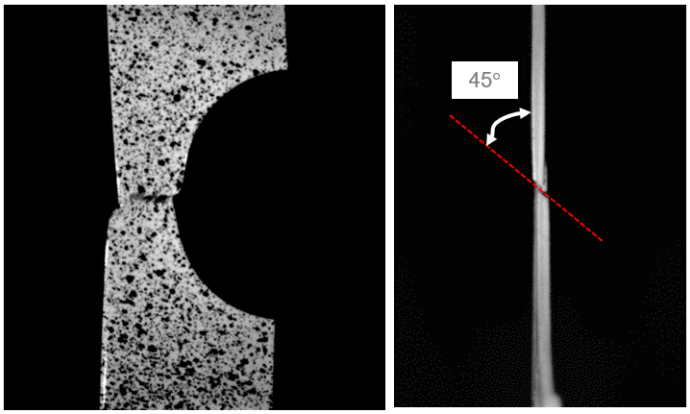

Figure 3.29: 45-degree crack observed in thickness plane (20 mm notch radius).

Additionally, the 0–degree samples, represented by blue colored points on the top plots in both figures, showed better formability than 90-degree or 45-degree samples. During testing it was also observed that the 5 mm notch radius samples, fractured with very less or no significant necking or thinning, hence fracturing at much lower strains than the 20 mm notch radius samples. Furthermore, it was observed that sheared edge specimens largely fractured with a clean 45-degree crack in the thickness plane which can be seen in Figures 3.28 and 3.29.

To observe effect of edge quality, fracture strains corresponding to both 20% and 30% of sheet thickness die clearance values were plotted on the same plot. Effect of notch radius plot can be seen in Figure 3.30. The triangles represent 20% die clearance while the points represent 30% die clearance values. It was discerned that since the triangles and the points were close to each other for each notch radius, both 20% and 30% die clearance samples fractured at similar strains. Figure 3.31 represents effect of orientation plot where it was further noted that the triangles and the points of the same color were close to each other in most cases.Here each color represented one of the three orientations 0, 90 and 45. Therefore, it was discerned that the edge quality did not have a significant effect on fracture strains. Both 20% and 30% die clearance value samples fractured at similar values of major and minor strains, suggesting that both held similar formability property.

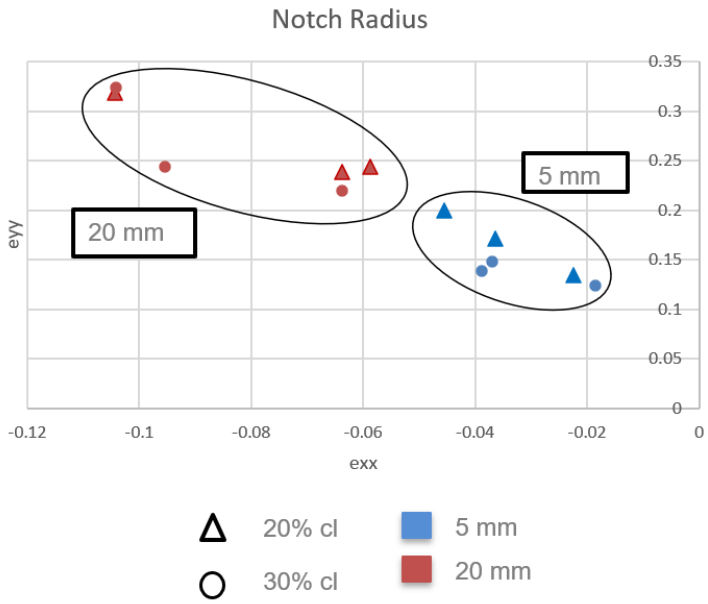

Figure 3.30: Effect of edge quality for sheared edge samples (notch radius).

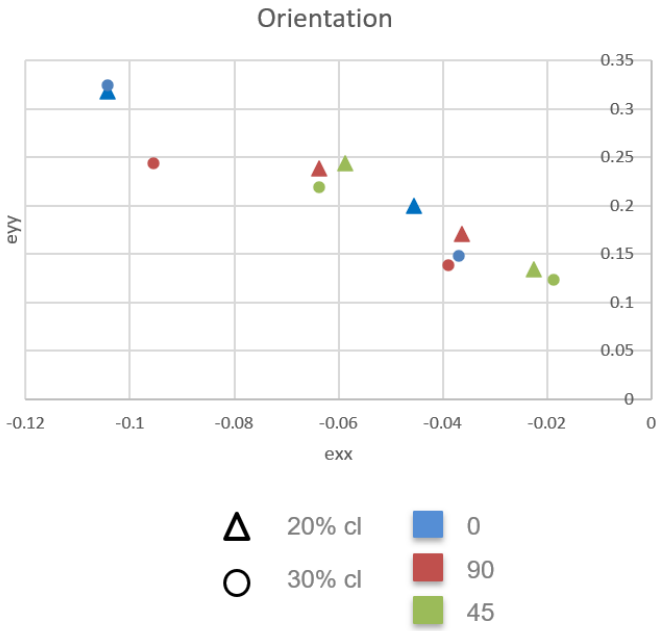

Figure 3.31: Effect of edge quality for sheared edge samples (Orientation).

3.4 Conclusions

3.4.1 Smooth-Edge Specimens

The tensile properties of steel grades used for testing notched specimens with smooth edge condition were recorded and specified. Experimental results pertaining to the steel grade DP 980 BARE, were used for numerical modelling and analysis in later chapters. Failure of the single notched machined edge specimens was mainly due to necking in both width and thickness directions, as the notched specimens experienced higher strains before fracture. The location of fracture was observed to be at the apex of the notch.

Observations pertaining to the effect of notch radius showed that smaller notch radius samples fractured at larger major and minor strains. Strain gradient plots plotted for the three notch radii samples showed that higher strain gradient (smaller notch radius) corresponded to better formability.

Furthermore, observations pertaining to the effect of material orientation showed that 90-degree specimens fractured at lower strains compared to 0-degree or 45-degree specimen of a particular notch radius for a steel grade. This observation for DP 980 BARE can be seen in Figure 3.23.

3.4.2 Sheared-Edge Specimens

Tensile properties of steel grades used for testing notched specimens with sheared/blanked edge condition were recorded and specified. The experimental results pertaining to the steel grade CR 780, were used for numerical modelling and analysis in later chapters. Failure of 5 mm notch radius specimens exhibited very less or no thinning/necking. Specimens fractured at the apex with a 45-degree crack seen from thickness direction.

Observations pertaining to the effect of notch radius for sheared-edge specimens contrasted with those of smooth-edged specimens. Higher notch radius samples fractured at larger strains, as seen in Figures 3.26 and 3.27 for 20% and 30% of sheet thickness die clearance values, respectively. Potential reason for this behavior was identified to be poor edge quality of sheared-edge samples since it was the only major difference between the two types of specimens. Further anal-

ysis could be performed by testing samples with wider range of die clearances, such as, from 5% to 30% which are typical in automotive forming industry.

Furthermore, the observations pertaining to the effect of material orientation for CR 780, showed that 0-degree specimens fractured at higher major strains when compared to 90-degree and 45-degree specimens of the corresponding notch radius for CR 780, which is depicted in Figures 3.26 and 3.27.

Samples exhibited similar fracture strain values corresponding to both 20% and 30% of sheet thickness die clearances. This is depicted in Figures 3.30 and 3.31, therefore effect of die clearance was found to be insignificant.

4. NUMERICAL MODELLING

In this chapter the details regrading numerical modelling part of the investigation were expounded. The finite element software package ABAQUS was used to perform all simulations. While performing experiments helped observe the failure behavior of various specimens and understand the effect of different sample parameters, conducting corresponding FEA simulations helped validate the modelling & analysis techniques and compare FEA output with experiments to investigate FEA predicted necking and fracture strains.

This chapter starts with explaining the modelling and analysis approach used, followed by details of tensile test simulations that were performed for DP 980 BARE and CR 780 steel grades, details of single notch specimen test simulations for the two steel grades and finally explicates vital results and conclusions.

4.1 Modelling and Analysis Approach

The approach used in this work involved validation of the simulation model using tensile tests and applying the same model to single notched geometry for comparing results with experimental observations of smooth and sheared edge notched specimens.

Tensile test simulations of DP 980 BARE and CR 780 were performed to validate the numerical model. Main inputs for this model were elastic modulus, plastic strains with corresponding stresses and stress ratios to incorporate anisotropy. These were obtained from true stress vs true strain plots and 2D DIC analysis. Stress ratios were computed from Lankford parameter (r) values acquired from DIC analysis. Strains were recorded at maximum load/start of necking (at UTS), of the 0-degree, 90-degree and 45-degree tensile specimens of the steel grades tested. Lankford parameter values utilized as input for ABAQUS simulations are listed in Table 3.9 and Table 3.10 for DP 980 BARE and CR 780 respectively. The stress-strain curve output, Lankford parameter and necking strains output from FEA simulations were compared to the experiments for validation. Later on, this material model was applied to the notched geometry and various simulations were run. The

results obtained were compared to limiting strains from single notch test experiments.

4.2 Tensile Test Simulations

4.2.1 Pre-processing and Analysis

Tensile tests were simulated in ABAQUS environment for DP 980 BARE and CR 780 material grades. The stress vs strain curve in both elastic and plastic regions and the Lankford parameter (r) calculated at necking accounted for main data points processed from experiments in the pre-processing stage.

To process the stress-strain data, load and displacement data collected during experiment was utilised. Engineering stress was first computed using the load data and area of specimen which was acquired by measuring the width and thickness before experiment. Table 4.1 provides the dimensions of specimens measured for three orientations of the two steel grades. To calculate strains, the "Extensometer" feature in the commercial 2D DIC software Correlated Solutions, was utilised. A gauge length of 50 mm in case of DP 980 BARE and 25 mm (sub-size) for CR 780 specimens was used. The "Extensometer" feature measured the strains over the required gauge length from the initial pull until the final fracture of the tensile specimen which were categorised as true strains. These engineering stress and true strain values were utilized to compute true stresses and the true stress vs true strain curves were plotted.

Table 4.1: Dimensions of tensile specimens of DP 980 BARE and CR 780.

Steel Grade	**Tensile Specimen Orientation**	**Width (mm)**	**Thickness (mm)**	**Area (mm^2)**
DP 90 BARE	0,90,45 degrees	12.5	1.5	18.75
CR 780	0,90,45 degrees	6	1.5	9

Later, the curve's data was utilized to compute Young's modulus, elastic strains and plastic strains, used as required inputs in ABAQUS. The yield strength and ultimate tensile strength were also determined as listed in Tables 3.2, 3.3, 3.4 and 3.6, 3.7, 3.8 for DP 980 BARE and CR 780

respectively. For planar anisotropy (in 2D), relation between stress ratios and strain ratios as per Hill's (1948) anisotropic plastic yield criterion referred from current ABAQUS manual, is shown in Equation 4.1. Here R_{11}, R_{22}, R_{33}, R_{12}, R_{23}, R_{13} represent stress ratios computed to be input in ABAQUS from the strain ratios r_0, r_{90} and r_{45} in three orientations. The stress ratios were input in ABAQUS under the "Plasticity" material modelling module. While simulating the 0-degree sample, appropriate direction in terms of material orientation was provided in ABAQUS in the "Orientations" tab. Similar procedure was followed for 90-degree and 45-degree specimens.

$$\begin{aligned} R_{11} &= R_{13} = R_{23} = 1 \\ R_{22} &= \sqrt{\frac{r_{90}(r_0+1)}{r_0(r_{90}+1)}} \\ R_{33} &= \sqrt{\frac{r_{90}(r_0+1)}{r_0+r_{90}}} \\ R_{12} &= \sqrt{\frac{3*r_{90}(r_0+1)}{(2*r_{45}+1)(r_0+r_{90})}} \end{aligned} \tag{4.1}$$

To obtain Lankford parameters from DIC, the logarithmic transverse and longitudinal strains (e_{xx} and e_{yy}) were obtained at UTS for tensile specimens. The picture of speckled tensile specimen at maximum load was identified and strain contouring was done to acquire strains in two perpendicular directions at the necking region. The "Point" feature in Correlated Solutions was monitored to extract these strains after analysis. This window consisted of the default smallest pixel value that was achieved for that particular strain analysis run. It was selected on the picture which corresponded to maximum load application (at UTS) near the region where necking occurred later in the test. The "Area of Interest" option was chosen during in DIC analysis to select the desired window.

Analysis in ABAQUS interface was done by modelling the part according to geometry and dimensions of the dog-bone tensile specimen tested experimentally. In case of DP 980 BARE, the standard ASTM tensile sample with 50 mm gauge length was modelled, while the sub-size specimen with 25 mm gauge length was utilized for CR 780. A "3D-Deformable" part with "Planar,

Shell" element was applied in both cases. To incorporate directional anisotropy, the right material orientation was provided in the "Orientations" tab. In the "Material Properties" section, under "Elasticity", properties of elastic modulus and Poisson's ratio were incorporated. Additionally, the stresses and corresponding plastic strains with the appropriate values of stress ratios under the "Potential" tab, were given in the "Plasticity" section.

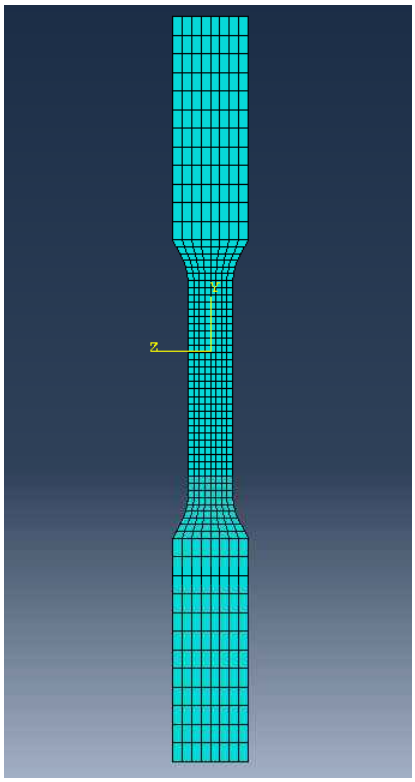

Figure 4.1: Meshing on tensile sample in ABAQUS interface.

On the "Step" tab a "Dynamic, Explicit" step was used to control the time increment value of 0.05 units with a run time of 1 unit for each analysis, while loading and boundary conditions were applied under the "Load and Boundary Conditions" section. Since displacement controlled simulation was being used for each case, a displacement value equivalent to the cross-head displacement in the experiment was used to deform the specimen. A dense mesh at the gauge length and courser mesh at the grips was provided, as seen in Figure 4.1. The element type S4R, a lin-

ear 4-node shell element with reduced integration and hourglass control was utilized. Structured "Quad" elements were provided throughout the geometry and manual seeding was done wherever required. Simulations were run after all necessary inputs were loaded.

4.2.2 Post-processing and Results

The data pertaining to von Mises stresses in longitudinal direction, logarithmic and plastic strains in longitudinal and transverse directions, section thickness strain and section thickness were extracted. The first and second time derivatives of section thickness strain were computed using central difference method and the double time derivative of thickness strain was plotted against time to identify the extreme points (minima points). The occurrence of necking was identified to have occurred when a sudden drop was observed in the double time derivative of thickness strain, originally performed for deep drawing processes [20]. Same procedure was applied here while the elements experiencing maximum strain in ABAQUS environment were monitored.

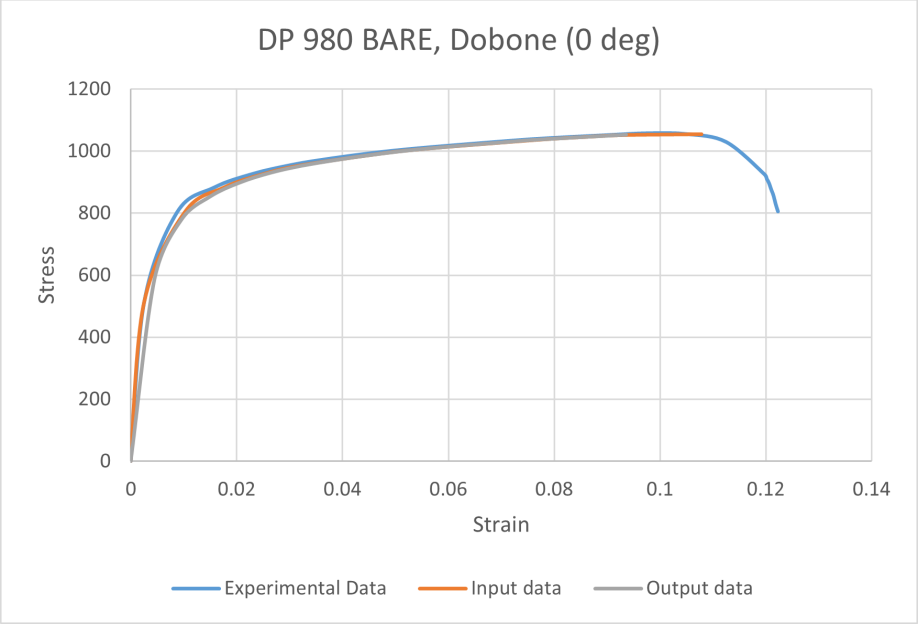

Figure 4.2: Stress vs Strain curve validation plot of DP 980 BARE.

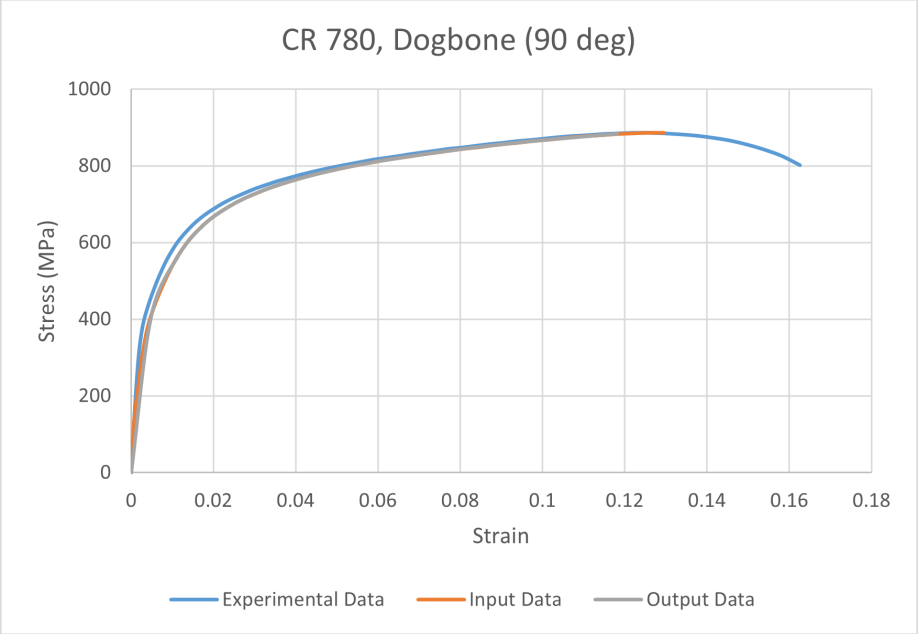

Figure 4.3: Stress vs Strain curve validation plot of CR 780.

Two minimum points were identified on the double time derivative of thickness strain curve. The same curve was plotted with longitudinal logarithmic strains (LE11) plot, extracted from ABAQUS to identify the longitudinal strain values at the minimum points. The first minimum corresponded to occurrence of diffuse necking and this strain was a close match to the experimental strain at UTS analysed using DIC. The second minimum was identified as that corresponding to occurrence of localized necking. A total of six tensile test simulations were performed, three for DP 980 BARE and CR 780 each, corresponding to the three orientations. Figure 4.2 and Figure 4.3 show the stress-strain curve validation plot of DP 980 BARE, 0-degree and CR 780, 90-degree specimens. Similar validation was done for other orientations and a good match was found in all cases.

Figure 4.4 and Figure 4.5 show the double time derivative of thickness strain plots for DP 980 BARE, 0-degree and CR 780, 90-degree specimens respectively. The longitudinal necking strain (LE11) is called out at the first minimum point observed on the second time derivative of thickness strain plot.

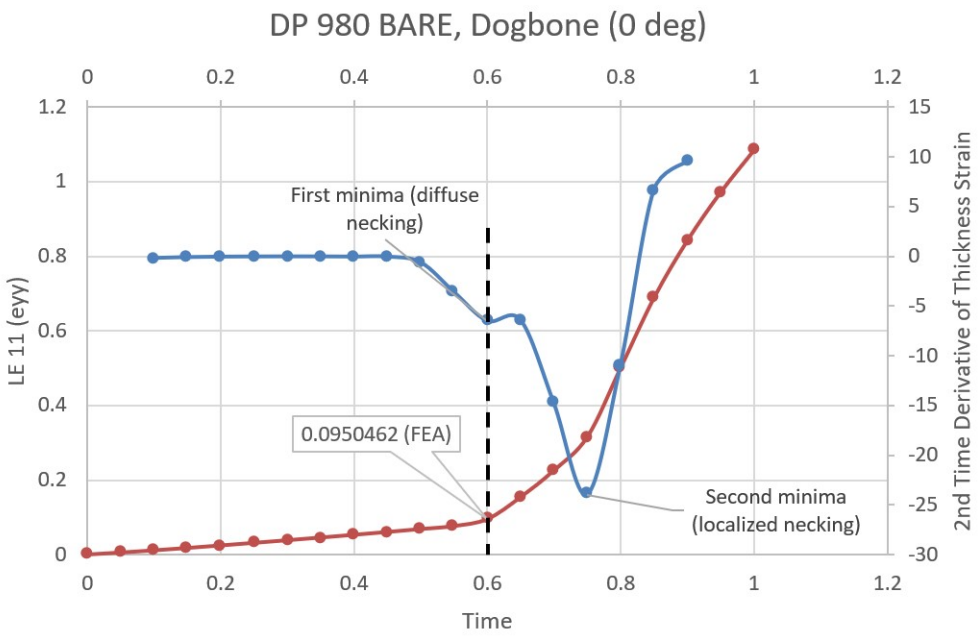

Figure 4.4: 2nd Time Derivative of Thickness Strain (blue) plotted with logarithmic Longitudinal Strain, LE11(red) vs Time for DP 980 BARE, 0 degree specimen.

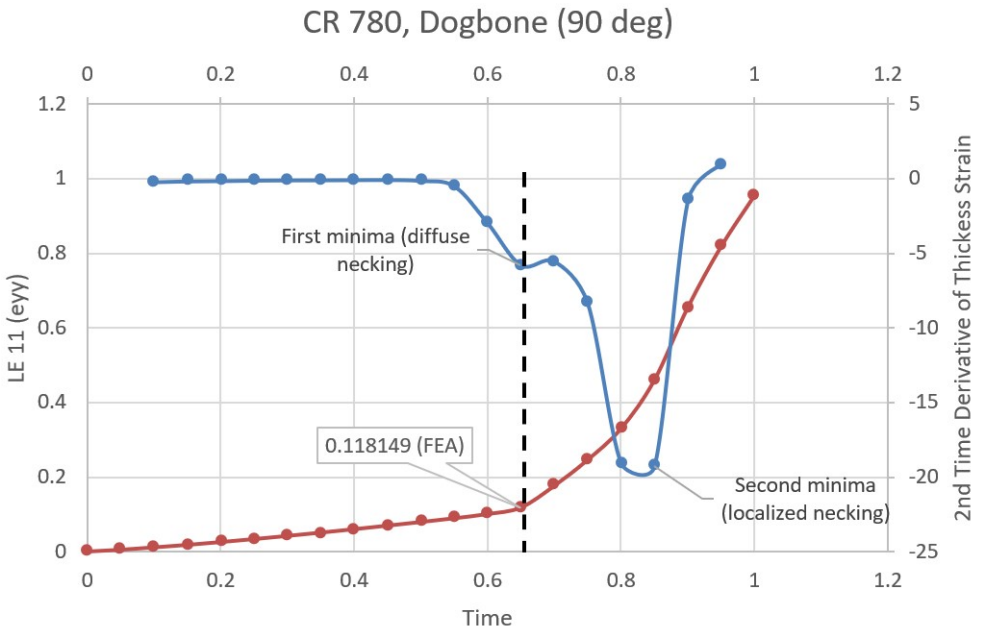

Figure 4.5: 2nd Time Derivative of Thickness Strain (blue) plotted with logarithmic Longitudinal Strain, LE11 (red) vs Time for CR 780, 90 degree specimen.

This value along with numerical transverse necking strain (LE22) were compared to strains analysed using DIC at UTS (start of necking). Table 4.2 summarises the results obtained for the two steel grades for all three orientations. Here Exp. e_{yy} and Num. e_{yy} represent experimental and numerical longitudinal strains respectively while Exp. e_{xx} and Num. e_{xx} represent the experimental and numerical transverse strains. A close match between the experimental and numerical necking strains from simulations was found, which helped validate the material modelling technique used to run the simulations thereafter.

Table 4.2: Experimental and numerical results of Lankford parameter (r), e_{yy} and e_{xx} strain values at necking (UTS), for DP 980 BARE and CR 780 tensile specimens.

Steel Grade	**Orientation**	**Exp. *r***	**Num. *r***	**Exp. e_{yy}**	**Num. e_{yy}**	**Exp. e_{xx}**	**Num. e_{xx}**
DP 980 BARE	0	0.790	0.789	0.0909	0.0951	-0.0401	-0.0413
DP 980 BARE	90	0.980	0.980	0.0755	0.0762	-0.0375	-0.0365
DP 980 BARE	45	1.030	1.028	0.0987	0.0955	-0.0499	-0.0468
CR 780	0	0.886	0.885	0.0902	0.0885	-0.0423	-0.0409
CR 780	90	0.920	0.919	0.1139	0.1181	-0.0545	-0.0559
CR 780	45	0.753	0.752	0.1170	0.1121	-0.0502	-0.0473

4.3 Single Notch Specimen Test Simulations

4.3.1 Pre-processing and Analysis

The same material model used in tensile test simulation was used to simulate notched specimens. Main inputs were r values and stress vs strain data in both "Elasticity" and "Plasticity" sections, same as tensile test simulations. A dense mesh was created near the apex of the notch, as shown in Figure 4.6 to smooth the extracted data since these elements were monitored to acquire required data to plot double time derivative plot as they experienced the highest stress. A combination of steel grades DP 980 BARE with smooth edge condition and CR 780 with sheared edge condition, and various orientations were selected to have a variety of results for analysis and observation.

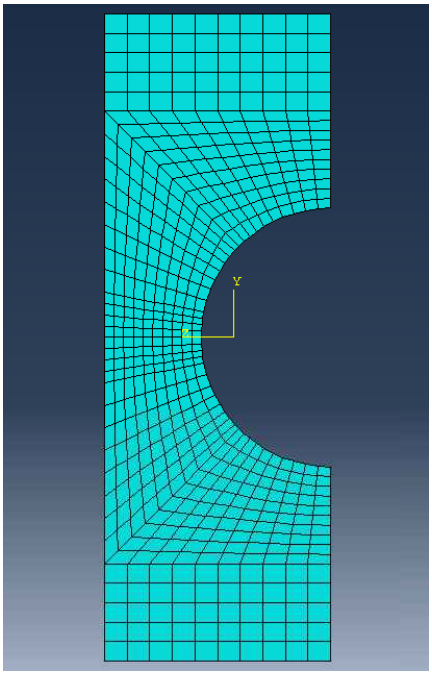

Figure 4.6: Meshing on notched (20 mm notch radius) sample in ABAQUS interface.

4.3.2 Post-processing and Results

Post running the simulations, the first and second time derivatives of section thickness strain for monitored elements were computed using central difference method and the double time derivative of thickness strain was plotted against time to identify the extreme points (minima points). Plots of both DP 980 BARE and CR 780 displayed only one prominent minima point, as opposed to the plot seen for tensile test simulations. Additionally, the behavior for DP 980 BARE (smooth-edge) was significantly different than CR 780 grade (sheared-edge). For DP 980 BARE, with all notch radii (10 mm, 30 mm and 50 mm), there was a slightly vague dip in the second time derivative curve and a prominent second minimum point was observed as displayed by the blue colored curve in Figure 4.7, while only one prominent minimum was observed for CR 780 as shown in Figure 4.8. Since only one distinguishable minimum point was observed for both steel grades (identified as point of localized necking in tensile test simulations), the localized necking strains were used for comparison with experimental results.

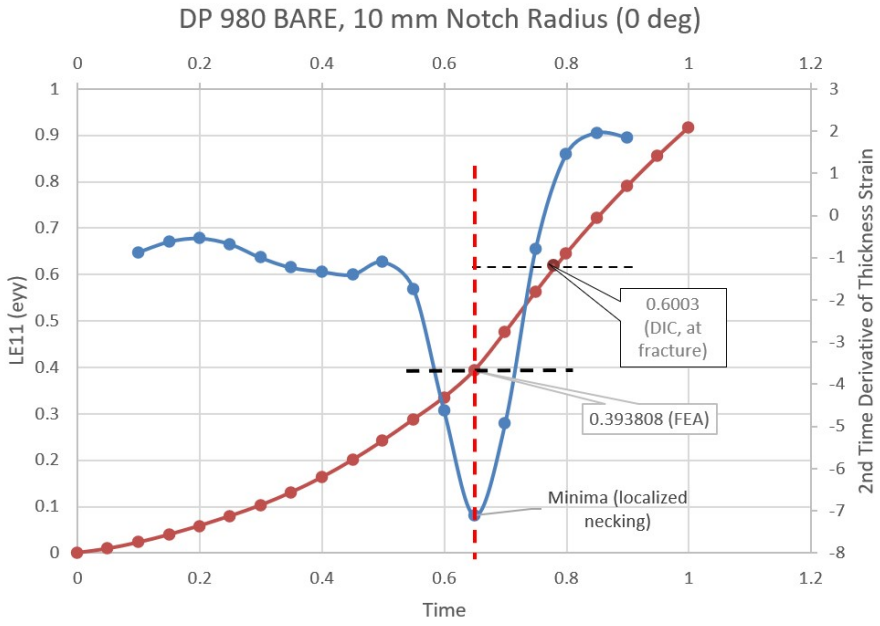

Figure 4.7: 2nd Time Derivative of Thickness Strain (blue) plotted with logarithmic Longitudinal Strain, LE11 (red) vs Time for DP 980 BARE, 10 mm notch (with smooth-edge), 0 degree specimen.

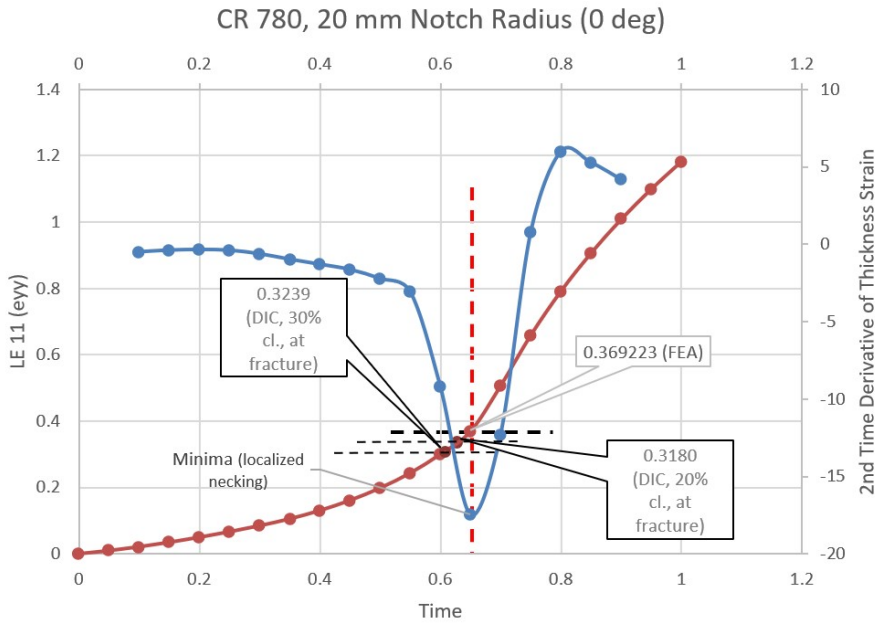

Figure 4.8: 2nd Time Derivative of Thickness Strain (blue) plotted with logarithmic Longitudinal Strain, LE11 (red) vs Time for CR 780, 20 mm notch (with sheared-edge), 0 degree specimen.

In Figures 4.7 and 4.8 the DIC analyzed fracture strains are marked along with FEA output. In Figure 4.7, for smooth-edge specimen, it was observed that the FEA predicted strains were conservative in nature since experimental fracture strain was higher that the limiting strain predicted numerically (localized necking strain). In case of sheared-edge, as seen in Figure 4.8, although the FEA predicted strain was substandard as DIC fracture strains for both 20% and 30% of sheet thickness die clearance values were lower than FEA result, these values were not very far from experimental fracture strains.

Table 4.3 summarises the results comparing the experimental and numerical limiting strain results. Here die clearance is expressed in terms of % of sheet thickness. The fifth column lists the experimental longitudinal fracture strains while the sixth column lists FEA predicted longitudinal localized necking strain for DP 980 BARE (smooth-edged) and CR 780 (sheared-edged) notched specimens. It can be discerned that FEA results for all smooth-edge samples were conservative since Exp. e_{yy} values were greater than Num. e_{yy}. However, Exp. e_{yy} values were lower than Num. e_{yy} for sheared-edge samples, hence the FEA prediction was substandard.

Table 4.3: Experimental and simulation results of e_{yy} strain values at failure, for DP 980 BARE and CR 780 notched specimens (Die cl. expressed as % of sheet thickness).

Steel Grade	**Notch Radius**	**Die cl.**	**Orientation**	**Exp. e_{yy} (fracture)**	**Num. e_{yy} (loc. neck)**
DP 980 BARE (smooth-edge)	10 mm	-	0	0.6003	0.3938
DP 980 BARE (smooth-edge)	30 mm	-	0	0.4857	0.3612
DP 980 BARE (smooth-edge)	30 mm	-	45	0.5045	0.3916
DP 980 BARE (smooth-edge)	50 mm	-	90	0.3882	0.3402
CR 780 (sheared-edge)	5 mm	20%	90	0.1709	0.3676
CR 780 (sheared-edge)	5 mm	30%	90	0.1381	0.3676
CR 780 (sheared-edge)	20 mm	20%	0	0.3180	0.3692
CR 780 (sheared-edge)	20 mm	20%	45	0.2433	0.3820
CR 780 (sheared-edge)	20 mm	30%	0	0.3239	0.3692
CR 780 (sheared-edge)	20 mm	30%	45	0.2194	0.3820

In order to investigate the relation between the FEA predicted and DIC analyzed fracture strains corresponding to the sheared-edge notched specimens, the longitudinal strain values were further analyzed. Since the FEA extracted strains for sheared-edge samples were higher that DIC strains, it was divided by the DIC strain to introduce a factor by which the FEA predicted strains might be away from experimental values. This factor was named as the Failure Strain Factor. Multiplying the FEA predicted strain with Failure Strain Factor rendered the actual strain at which the sheared-edge samples fractured. For the CR 780, 20 mm notch radius, 0-degree specimen, Failure Strain Factor was close to 0.870, which was averaged for both die clearance values. These results are shown in Table 4.4. Equation 4.2 displays computation equation for Failure Strain Factor.

Table 4.4: Failure Strain Factor for sheared-edge sample CR 780, 20 mm notch radius (Die cl. expressed as % of sheet thickness).

Steel Grade	**Notch Radius**	**Die cl.**	**Orientation**	**Exp. e_{yy} (frac)**	**Num. e_{yy} (loc. neck)**	**Failure Strain Factor**
CR 780 (sheared-edge)	20 mm	20%	0	0.3180	0.3692	0.8617
CR 780 (sheared-edge)	20 mm	30%	0	0.3239	0.3692	0.8777

$$\text{Failure Strain Factor} = \frac{Exp.e_{yy}(\text{fracture})}{Num.e_{yy}(\text{localized necking})} \tag{4.2}$$

Existence of this strain disparity in sheared-edge samples could be a result of effect of blanked edge/poor edge quality of the samples. Additionally, since the FEA model did not incorporate the edge quality itself, simulating these samples was similar to simulating smooth edge samples in the ABAQUS environment. Stress concentration at the microcracks due to microvoids and burr, in the sheared edge could also be likely reasons leading to the mismatch between FEA predicted and

experimental strains. Hence, further investigation into the stress-based failure criteria and fracture mechanics aspect might be needed for accurate understanding of the this fracture behavior.

4.4 Conclusions

4.4.1 Tensile Test Simulations

Tensile tests were simulated for DP 980 BARE and CR 780, in three material orientation directions, in FEA code ABAQUS interface with required material property inputs of elastic modulus, plastic stains and corresponding stresses, and stress ratios to incorporate anisotropy. The true stress-true strain data was input into ABAQUS from true stress vs true strain curve obtained using load-displacement data and 2D DIC strain analysis, for tensile tests. Elements which experienced highest strains were monitored to extract logarithmic & plastic, longitudinal & transverse strains, longitudinal stresses and section thickness strain data, for post processing.

The stress-strain curves were validated as shown in Figures 4.2 and 4.3. The second time derivative of thickness strain method was used to identify strain at necking [20]. Two minimum points were identified on the 2nd Time Derivative of Thickness Strain vs Time plot. The same curve was plotted with longitudinal logarithmic strains (LE11), extracted from ABAQUS to identify the longitudinal strains at the minimum points. First and second minimum points were identified to be corresponding to the occurrence of diffuse and localized necking respectively. The diffuse necking strain value recognized at first minima was a close match to the strain at UTS analysed using DIC, as seen in Figures 4.4 and 4.5.

Experiments and simulations showed good correlation, both in terms of stress vs strain curve and necking strains match, in tensile test simulation runs as summarized in Table 4.2. Therefore, the FEA modelling technique was established.

4.4.2 Single Notched Specimen Test Simulations

Single notched tests were simulated for DP 980 BARE and CR 780, with various notch radii, in three material orientation directions, in ABAQUS interface with required material property inputs of elastic modulus, plastic stains and corresponding stresses, and stress ratios to incorporate

anisotropy. The true stress-true strain data was input into ABAQUS from true stress vs true strain curve obtained using load-displacement data and DIC strain analysis, for tensile tests. Elements which experienced highest strains were monitored to extract logarithmic & plastic longitudinal & transverse strains, longitudinal stresses and section thickness strain data, for post processing.

The second time derivative of thickness strain method was used to identify strain at localized necking point, as only the second prominent minima point (corresponding to localized necking) could be identified in the plot for notched specimens. The same curve was plotted with longitudinal logarithmic strains (LE11), extracted from ABAQUS to identify the longitudinal strain values at the minima point as seen in Figures 4.7 and 4.8. It was discerned that FEA limiting strains for smooth-edged notched samples provided conservative results since experimental fracture strains were greater than numerically predicted localized necking strains. In case of sheared edge samples, the experimental fracture strains were lower than numerically predicted localized necking strains, hence the FEA prediction were substandard in this case. The results for both smooth-edge and sheared-edge specimens are summarized in Table 4.3.

Further investigate for sheared-edge samples revealed the possibility of an empirical relation between the FEA predicted and DIC analyzed longitudinal fracture strains. The FEA fracture strain was divided by the experimental DIC strain to introduce Failure Strain Factor by which the FEA strains were away from experimental value. By multiplying the FEA predicted strain with this factor, the actual strain at which the sheared-edge samples fractured could be predicted. For the CR 780, 20 mm notch radius, 0-degree specimen, the value of Failure Strain Factor was close to 0.870, averaged over both die clearance values, as summarized in Table 4.4.

5. SUMMARY AND CONCLUSIONS

5.1 Experimental Investigation

The tensile properties of steel grades used for testing notched specimens with smooth and sheared edge conditions were recorded and specified. Experimental results pertaining to the steel grade DP 980 BARE and CR 780 were used for numerical modelling and analysis.

The failure of the single notched smooth-edge specimens (without burrs and micro-cracks) was mainly due to necking in both width and thickness directions, at the apex, as the notched specimens experienced higher strains before fracture. Smaller notch radii samples fractured at larger major and minor strains suggesting that notch radius size was inversely proportional to formability property of the steel grade. Strain gradient plots were plotted for the three notch radii samples tested, which suggested that higher strain gradient (smaller notch radius), corresponded to better formability. The 90-degree specimens fractured at lower strains than 0-degree or 45-degree specimen of a particular notch radius. This accounted for the effect of material orientation.

The failure of single notched sheared-edge, 5 mm notch radius specimens exhibited less thinning/necking before fracture while all specimens cracked at the apex with a 45-degree crack when seen from thickness direction. The effect of notch radius for sheared-edge specimens contrasted with that of smooth-edged samples. Higher notch radius samples fractured at larger strains for both 20% and 30% of sheet thickness die clearance values in case of sheared-edge samples. The potential reason for this contrasted response was identified to be poor edge quality as compared to smooth-edge samples since this was the main difference between the two types, hence edge quality played a critical role in fracture behavior of sheared-edge AHSS samples.

The 0-degree specimens fractured at higher major strains when compared to 90-degree and 45-degree specimens of the corresponding notch radius for CR 780. Strains corresponding to the 20% of sheet thickness die clearance samples were not far from 30% clearance ones, hence effect of die clearance was found to be insignificant for sheared-edge samples.Further analysis could be

performed by testing samples with wider range of die clearances, such as, from 5% to 30% which are typical in automotive forming industry. This could also help clarify the contrasted response of sheared and smooth-edge samples pertaining to effect of notch radius.

5.2 Numerical Modelling

Tensile tests and single notched specimen tests were simulated for DP 980 BARE and CR 780, in three material orientation directions and various notch radii, in FEA code ABAQUS interface. Required material property inputs of elastic modulus, plastic stains, corresponding stresses and stress ratios to incorporate anisotropy, were provided subsequently. The true stress-true strain data was input into ABAQUS from true stress vs true strain curve obtained using load-displacement data and 2D DIC strain analysis of tensile tests. Meshed elements experiencing highest strains were monitored to extract logarithmic & plastic, longitudinal & transverse strains, longitudinal stresses and section thickness strain data, for post processing.

Second time derivative of thickness strain method was used to identify strain at necking. Two minima points were identified on the 2nd Time Derivative of Thickness Strain vs Time plot in tensile tests simulations. The first and second minima points corresponded to occurrence of diffuse and localized necking respectively. Diffuse necking strain value was a close match to the strain at UTS analysed with DIC in tensile tests. Experiments and simulations showed good correlation, both in terms of match in results of stress vs strain curve output and necking strains for tensile test simulations which helped establish the FEA modelling technique.

For single notched specimen test simulations, second time derivative of thickness strain method was used to identify only one prominent minima point that corresponded to localized necking strain in tensile test simulations. Smooth-edged notched samples provided conservative results since experimental fracture strain values were higher than numerically predicted limiting strains. Whereas, sheared edge samples provided substandard prediction since experimental fracture strain values were lower than numerically predicted limiting strains.

Further investigation on sheared-edge samples revealed potential empirical relation between the FEA predicted longitudinal limiting strain and DIC analyzed (actual) longitudinal fracture

strain. A new factor called the Failure Strain Factor was introduced. By multiplying the FEA predicted strain with this factor, the experimental strain at which the sheared-edge samples fractured, could be predicted. For the CR 780, 20 mm, 0-degree specimen, this factor was close to 0.870, which was averaged for both die clearance values. Additional study into the stress-based failure criteria and approach from fracture mechanics side might be required to look into aspects such as, stress concentration in microcracks due to micro-voids and the effect of burr, for a more accurate interpretation of the FEA results pertaining to sheared-edge samples.

REFERENCES

[1] E. Billur and P. D.-i. T. Altan, "Challenges in Forming Advanced High Strength Steels," *New Developments in Sheet Metal Forming*, pp. 285–304, 2010.

[2] H. C. Shih, C. Chiriac, and M. F. Shi, "The effects of AHSS shear edge conditions on edge fracture," *ASME 2010 International Manufacturing Science and Engineering Conference, MSEC 2010*, vol. 1, pp. 599–608, 2010.

[3] N. Baluch, Z. M. Udin, and C. S. Abdullah, "Advanced High Strength Steel in Auto Industry: an Overview," *Engineering, Technology & Applied Science Research*, vol. 4, no. 4, pp. 686–689, 2014.

[4] S. Huang, Y. x. Zhao, and C. f. He, "Shear fracture of advanced high strength steels," *Journal of Iron and Steel Research International*, vol. 21, no. 10, pp. 938–944, 2014.

[5] H. Kim, J. Shang, J. Dykeman, A. Samant, and C. Hoschouer, "Practical Evaluation and Prediction of Edge Cracking in Forming Advanced High Strength Steels (AHSS)," *SAE Technical Papers*, vol. 2017-March, no. March, 2017.

[6] M. Feistle, R. Golle, and W. Volk, "Determining the Influence of Shear Cutting Parameters on the Edge Cracking Susceptibility of High-strength-steels Using the Edge-fracture-tensile-test," *Procedia CIRP*, vol. 41, pp. 1078–1083, 2016.

[7] H. Kim, a. Bandar, Y.-P. Yang, J. Sung, and R. Wagoner, "Failure Analysis of Advanced High Strength Steels (AHSS) during Draw Bending," *IDDRG: Mat. Prop. Data for More Effective Num. Anal.*, no. June, pp. 1–12, 2009.

[8] H. Yoshida, K. Sato, T. Matsuno, T. Yoshida, Y. Takahashi, and J. Nitta, "Evaluation and improving methods of stretch flangeability," *Nippon Steel Technical Report*, no. 103, pp. 18–24, 2013.

[9] J. Dykeman, S. Malcolm, B. Yan, J. Chintamani, G. Huang, N. Ramisetti, and H. Zhu, "Characterization of edge fracture in various types of advanced high strength steel," *SAE 2011 World Congress and Exhibition*, no. Dic, pp. 1–11, 2011.

[10] P. Larour, H. Schauer, J. Lackner, and E. T. Till, "Edge crack Simulation with the modular 'smiley' forming tool," *International Deep Drawing Research Group Conference*, no. Figure 2, 2016.

[11] X. Chen, J. Sun, and X. Zhu, "Simulation Technique for Pre-forming of AHSS Edge Stretching," *12th International LS-DYNA Users Conference*, no. 3, pp. 1–12, 2012.

[12] M. F. Shi and J. C. Gerdeen, "Effect of strain gradient and curvature on forming limit diagrams for anisotropic sheets," *Journal of Materials Shaping Technology*, vol. 9, no. 4, pp. 253–268, 1991.

[13] Y. Li, M. Luo, J. Gerlach, and T. Wierzbicki, "Prediction of shear-induced fracture in sheet metal forming," *Journal of Materials Processing Technology*, vol. 210, no. 14, pp. 1858–1869, 2010.

[14] D. Frómeta, M. Tedesco, J. Calvo, A. Lara, S. Molas, and D. Casellas, "Assessing edge cracking resistance in AHSS automotive parts by the Essential Work of Fracture methodology," *Journal of Physics: Conference Series*, vol. 896, no. 1, pp. 0–8, 2017.

[15] D. Casellas, A. Lara, D. Frómeta, D. Gutiérrez, S. Molas, L. Pérez, J. Rehrl, and C. Suppan, "Fracture Toughness to Understand Stretch-Flangeability and Edge Cracking Resistance in AHSS," *Metallurgical and Materials Transactions A: Physical Metallurgy and Materials Science*, vol. 48, no. 1, pp. 86–94, 2017.

[16] N. Pathak, C. Butcher, M. J. Worswick, E. Bellhouse, and J. Gao, "Damage evolution in complex-phase and dual-phase steels during edge stretching," *Materials*, vol. 10, no. 4, pp. 1–29, 2017.

[17] A. R. Safikhani, R. Hashemi, and A. Assempour, "The strain gradient approach for determination of forming limit stress and strain diagrams," *Proceedings of the Institution of Mechanical Engineers, Part B: Journal of Engineering Manufacture*, vol. 222, no. 4, pp. 467–483, 2008.

[18] C. P. Nikhare, "Experiment and predictions of strain and stress based failure limits for advanced high strength steel0," *Materials Today: Proceedings*, vol. 5, no. 1, pp. 261–267, 2018.

[19] X. Chen, K. Chen, and L. Smith, "Pre-forming effects on AHSS edge cracking," *AIP Conference Proceedings*, vol. 1383, pp. 792–799, 2011.

[20] H. Chalal and F. Abed-Meraim, "Numerical predictions of the occurrence of necking in deep drawing processes," *Metals*, vol. 7, no. 11, 2017.

[21] J. D. Patel and K. D. Maniya, "A Review on: Wire cut electrical discharge machining process for metal matrix composite," *Procedia Manufacturing*, vol. 20, pp. 253–258, 2018.

[22] ASTM E8, "ASTM E8/E8M standard test methods for tension testing of metallic materials 1," *Annual Book of ASTM Standards 4*, no. C, pp. 1–27, 2010.

[23] G. Quino, Y. Chen, K. R. Ramakrishnan, F. Martínez-Hergueta, G. Zumpano, A. Pellegrino, and N. Petrinic, "Speckle patterns for DIC in challenging scenarios: Rapid application and impact endurance," *Measurement Science and Technology*, vol. 32, no. 1, 2021.

APPENDIX A

1. The Major Strain (e_{yy}) vs Minor Strain (e_{xx}) plots in Experimental Investigation section were plotted based on one repeat of each material sample.

2. The width of each sample was kept constant at 10 mm for smooth-edge and 15 mm for sheared-edge specimens as shown in Figures A.1 and A.2, respectively.

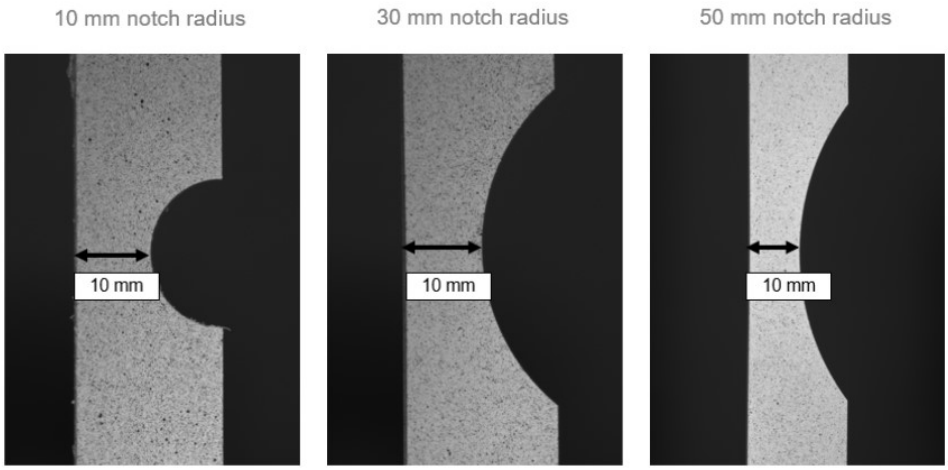

Figure A.1: Actual width of smooth-edge specimens.

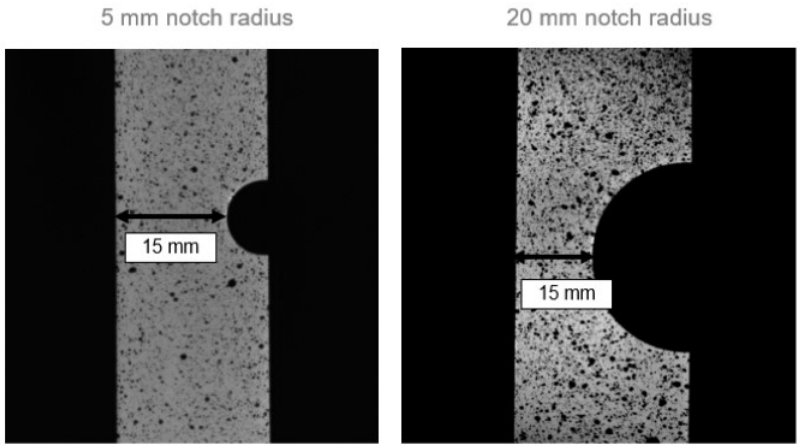

Figure A.2: Actual width of sheared-edge specimens.